UNIVERSITÀ DEGLI STUDI DI PADOVA

DIPARTIMENTO DI FISICA E ASTRONOMIA "G. GALILEI"

CORSO DI LAUREA MAGISTRALE IN

ASTRONOMIA

TESI DI LAUREA MAGISTRALE

Binaries among multiple populations in the young LMC cluster NGC 2164

Relatore: Dott. MILONE ANTONINO
Correlatrice: Dott.ssa MARINO ANNA FABIOLA

Laureando: JEAN EPHREM NASTASIO
Matricola: 1205772

ANNO ACCADEMICO 2019/2020

"Le cose sono unite da legami invisibili.
Non puoi cogliere un fiore senza turbare una stella."

- Galileo Galilei -

Contents

List of Figures

List of Tables

Abstract

In the past few years, young star clusters of both Magellanic Clouds have been found to be complex stellar systems. In addition to the extended main-sequence turn-offs (eMSTOs), common among intermediate-age clusters, split MSs have been observed. These discoveries have challenged the traditional picture that their Color Magnitude diagrams are similar to isochrones. Different scenarios have been proposed to understand the origin of the eMSTO and the split MSs. The main ones are the *age-spread* scenario, where the eMSTO is the result of prolonged star formation, and *rotation-spread* scenario, which assumes that all stars are coeval but exhibit different rotation rates. In the context of the rotational hypothesis, braking of stellar rotation induced by tidal interactions in binary systems has been proposed as responsible for the double main sequences.

In this thesis I exploit *Hubble Space Telescope* high precision photometry to constrain, for the first time, the frequency of binaries among multiple populations in NGC 2164. To do this, I apply a new method which is based on the comparison of multi-band photometry of binary stars and grids of simulated diagrams of artificial binary stars. My discovery of a prevalence of binaries among the blue MS corroborates the connection between binaries and split MSs, thus supporting the rotational scenario. I also report the discovery of a singular feature in the upper part of the CMD, hinting for a triple sequence.

Riassunto

Una delle scoperte più affascinanti degli ultimi anni riguarda il fatto che gli ammassi giovani di entrambe le Nubi di Magellano sono sistemi stellari complessi. In aggiunta ad un turn-off esteso della sequenza principale (eMSTO), comune tra gli ammassi di età intermedia, è stata osservata anche una doppia sequenza principale (split MS). Queste scoperte hanno rivoluzionato l'idea tradizionale per cui i diagrammi Colore-Magnitudine di questi ammassi sono simili a delle isocrone. Sono stati proposti diversi scenari per capire l'origine dell'eMSTO e della doppia MS. I principali sono quello delle variazioni di età, per cui l'eMSTO è il risultato di una formazione stellare prolungata, e lo scenario della rotazione, il quale assume che tutte le stelle siano coeve ma che abbiano diverse velocità di rotazione. Nell'ambito dell'ipotesi rotazionale, il frenamento della rotazione stellare indotto da interazioni mareali in sistemi binari sarebbe il principale responsabile per la doppia sequenza principale.

In questa tesi sfrutto dati fotometrici di alta precisione del telescopio spaziale Hubble per determinare, per la prima volta, la frequenza delle binarie tra le popolazioni multiple in NGC 2164. A tale scopo, applico un nuovo metodo basato sul confronto della fotometria multi-banda delle stelle binarie con una griglia di diagrammi simulati di binarie artificiali. La mia scoperta di una prevalenza di binarie nella sequenza principale blu conferma il nesso fra binarie e doppia MS, e quindi supporta lo scenario relativo alla rotazione. Riporto anche la scoperta di una nuova caratteristica nella parte alta del diagramma Colore-Magnitudine, che suggerisce l'esistenza di una sequenza tripla.

CHAPTER 1

Introduction

1.1 Multiple Stellar Populations in Globular Clusters

Since the time of their discovery and of the first studies, Globular Clusters (GCs) have been considered prototypes of Simple Stellar Populations (SSPs), composed of stars with the same age and chemical composition. Based on this assumed simplicity, GCs have been exploited as ideal laboratories for stellar formation and evolution. Being among the oldest objects, Galactic GCs provide information on the early phases of the Universe. Moreover, these ancient stellar systems may have provided a role in the chemical enrichment of the pristine interstellar medium and in the assembly of the halo of galaxies.
With the advent of high-resolution photometry this assumption of simplicity has been challenged and eventually set apart, but in spite of a better understanding some important questions still remain open and many more have risen. In the past decades with the huge improvements offered by the *Hubble Space Telescope*, both as an increased imaging resolution and as new pass-band observation possibilities (i.e. the ultraviolet spectral region precluded to ground observations), the study of GCs has pointed out the presence of Multiple Populations (MPs), efficiently identified in appropriate Color Magnitude Diagrams (CMDs: many examples are shown in this thesis, as in figure 1.3) or in the pseudo two color diagrams called "Chromosome Maps" (Milone et al. 2015b) by means of appropriate combinations of filters from the ultraviolet, visible and near-infrared portions of the spectrum.
One of the main open questions on the topic concerns the formation of stars inside GCs, and how MPs with different properties may originate from successive episodes of stellar formation or may evolve differently from an initial more homogeneous population. Formally, the *multi-populations* definition refers to distinct stellar populations that have differences in their age, and not to the differentiation they may experience in the subsequent evolutionary history; this could introduce some ambiguity in the scenario where the observed differences between populations are due to other properties but age, as it will be described in the following sections.
Recalling the studies of MPs in old globular clusters, according to one of the most accreditate scenarios a first generation of stars, called 1G, originates from the primordial cloud and pollutes the inter-stellar medium of the cluster in which a sec-

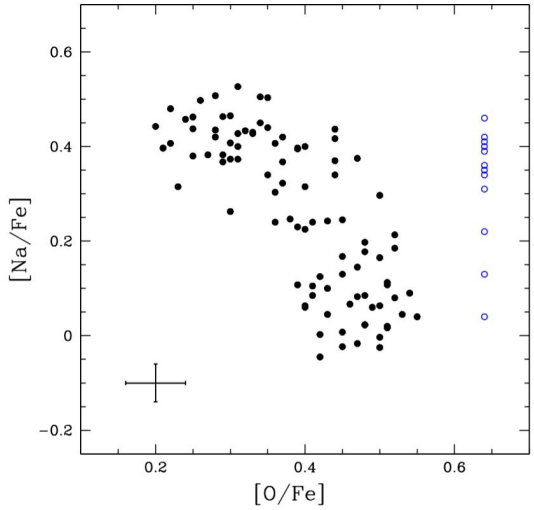

Figure 1.1: [Na/Fe] versus [O/Fe] abundance ratios in M4 display a clear anti-correlation, from which is possible do separate different populations. Figure taken from (Marino et al. 2008).

ond generation of stars, 2G, forms at a later time. This second generation is then composed of stars with a chemical composition that does not reflect the elements' abundances of the gas cloud from which the cluster was originated; in particular 2G's stars are depleted in Carbon (C) and Oxygen (O), but enriched in Nitrogen (N), Helium (He) and other elements like, Sodium (Na). Indeed, these chemical abundances allow to derive some anti-correlations that separate the two, or more, populations. An example of the clear Na-O anti-correlation is shown in figure 1.1 taken from (Marino et al. 2008).

1.2 Multiple populations in young clusters

It is currently well established that the MPs phenomenon is a common feature among all old GCs: it may present itself with different levels of complexity, but these objects cannot be considered a SSP anymore. It may be supposed that intermediate-age $(1 - 2Gyr)$ and, even more, young $(< 1Gyr)$ clusters are the simpler counterpart of older and hence more evoluted GCs.

Yet their study, mainly based on clusters from the Large Magellanic Cloud (LMC) and Small Magellanic Cloud (SMC) provided evidence of their CMDs being inconsistent with a SSP as well, with peculiar features leading to new hypothesis on the formation of multi-populations scenario; although in these young and intermediate-age clusters chemical variations between populations are much lower than in older clusters suggesting a second generation formation scenario that is less dependent on first generation polluters (Martocchia et al. 2018). Among the noticeable features in these clusters' CMDs are an extended Main Sequence Turn Off (eMSTO) and a split Main Sequence.

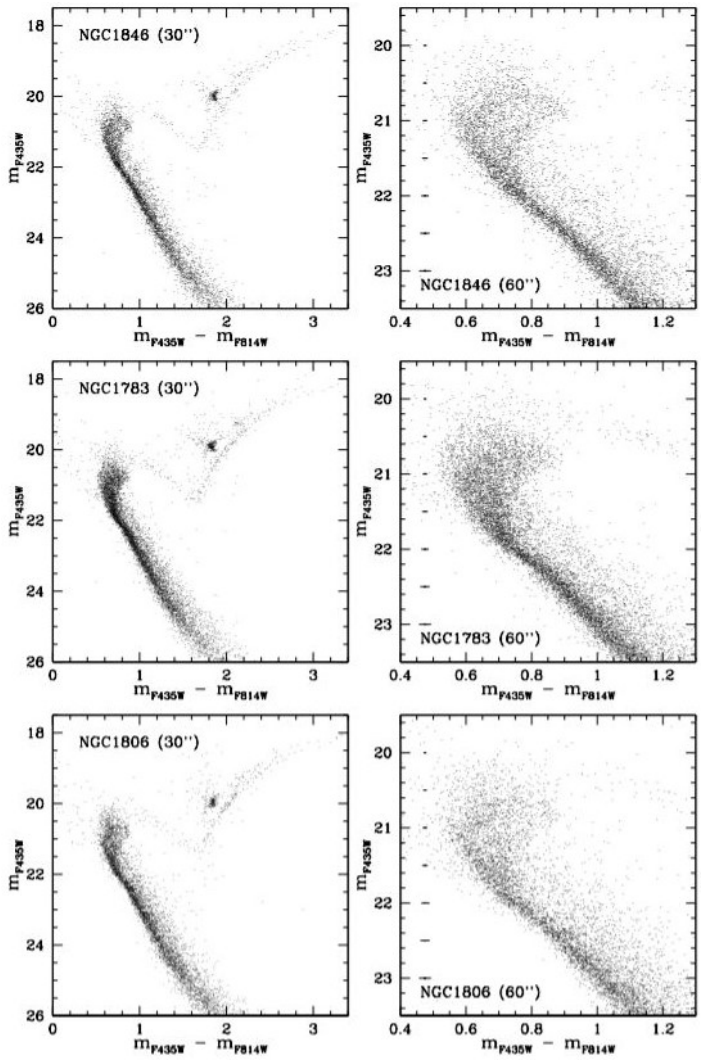

Figure 1.2: CMDs of three LMC intermediate-age star clusters. The second column shows in detail the extended-MSTO region with photometric uncertainties indicated on the left. Figure taken from (Mackey et al. 2008).

1.2.1 eMSTO and double MS

Since its discovery by (Mackey et al. 2007), extended Main Sequence Turn Off has been found to be a typical feature for massive intermediate-age clusters in Magellanic Clouds (MCs), suggesting a prolonged star formation history and the presence of multiple stellar populations (e.g. D'Antona et al. 2017, 2018; Milone et al. 2016) with age differences up to several hundreds million years for intermediate-age clusters. This possibility has been further supported by the evidence of dual red clumps indicating that the system is not consistent with a single isochrone (Girardi et al. 2009). Examples of this eMSTO can be seen in image 1.2 taken from (Mackey et al. 2008). The right-hand column of this figure zooms on the extended turn off region to show the evident spread in color at this magnitude level. The age spread suggested by this feature could be considered in analogy with the different star formation epochs giving birth to the multiple populations in old GCs (Piotto et al. 2015), for

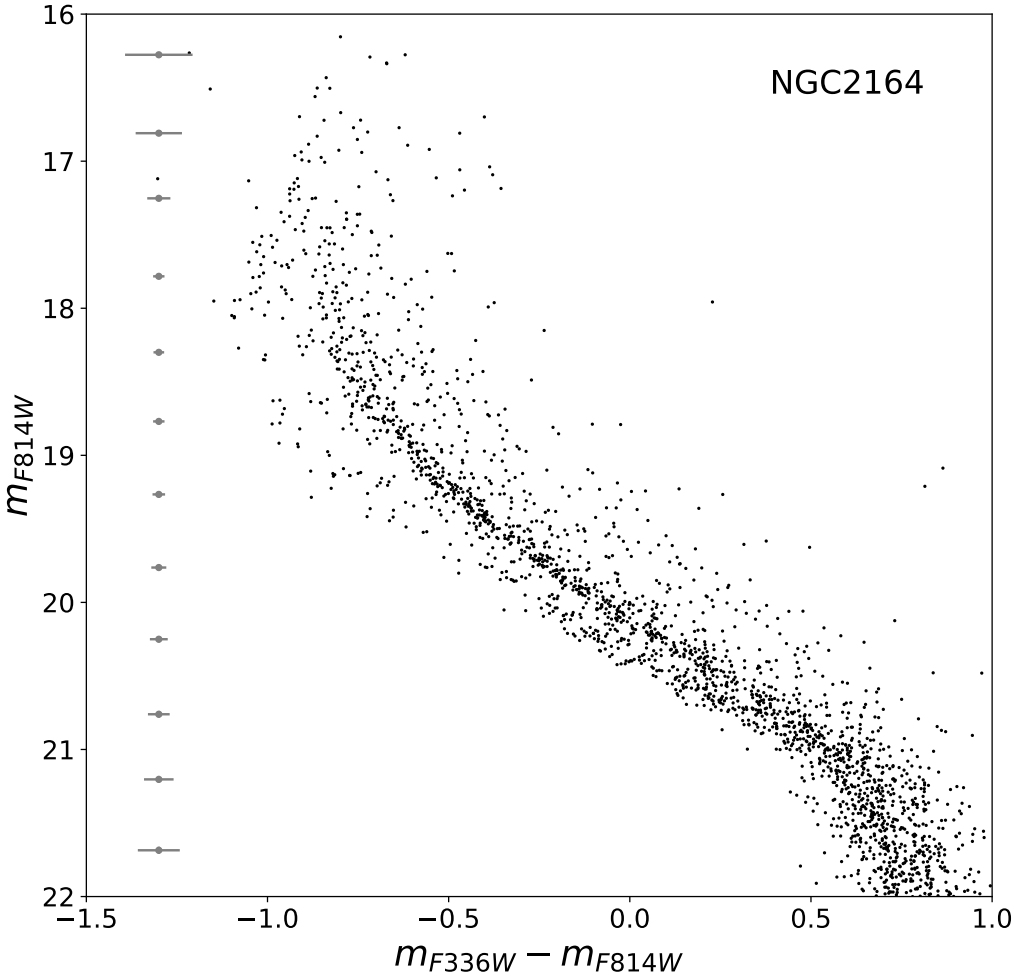

Figure 1.3: $m_{F336W} - m_{f814W}$ versus m_{F814W} CMD of the young LMC cluster NGC 2164. Photometric uncertainties are indicated on the left.

which successive populations with different chemical abundances generate out of the gas clouds enriched in chemical elements by first-generation stars.

In more recent years a split Main Sequence has been discovered as a new puzzling characteristic in young clusters CMDs (Milone et al. 2015a, D'Antona et al. 2015). In figure 1.3 is shown the $m_{F336W} - m_{f814W}$ versus m_{F814W} CMD of NGC 2164, the young cluster analysed in this work. This feature cannot be imputed to age or metallicity differences, as initially suggested (Milone et al. 2015a), but it is consistent with rapidly rotating stellar models for the "red" and more populated MS (rMS) and with slowly rotating stellar model for the "blue" and less populated MS (bMS), although some smaller age spread could still be requested to better reproduce the upper part of the blue MS with isochrones (see figure 1.6).

From observations it is noticeable that the two MSs are no longer split at the magnitude where the main sequence shows a kink: this it due to the appearance of convective surface layers at $T_{eff} < 7000K$ (D'Antona et al. 2002). Indeed, there is a strong connection between the rotational evolution and the nuclear burning stages of a star: the transport of angular momentum through the stellar layers is linked to the internal chemical mixing which in turn affects the evolutionary time-scales for

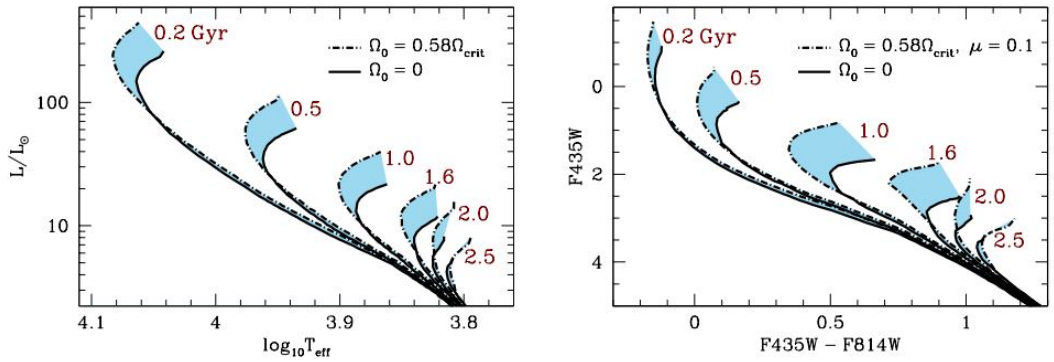

Figure 1.4: Extension of the turn off region, delimited by a rotating and non-rotating isochrone, in young and intermediate-age clusters. Image taken from (Brandt et al. 2015).

the H-core burning phase. Because of this mixing the convective core is enriched in hydrogen and extends its lifetime. The effect on stellar evolution is that stars with the same mass but different rotation rates evolve with non-identical time-scales and hence show a different turn-off luminosity, from which the extended main sequence turn-off originates.

1.2.2 Age-spread scenario

In the *age-spread* scenario, multiple stellar populations may be formed in a cluster due to a prolonged star formation history or to successive separated episodes. In MC clusters the age spread can span over several hundreds millions years. To trigger the formation of a second stellar population there must be enough gas in the cluster and different mechanisms can provide it, like the merging of young clusters with giant molecular clouds and the accretion of ambient gas by the clusters themselves. Obviously the clusters must be massive enough to retain the pristine and chemically enriched gas preventing its loss due to supernovae and stellar winds ejecta. This last point in particular has been treated by (Goudfrooij et al. 2014) looking for a correlation between the age and the age-spread of clusters, and accordingly between the age-spreads and the cluster masses. This scenario is challenged by the fact that in intermediate-age and young clusters there is no spectroscopic evidence of O and Na variations (Mucciarelli et al. 2011). It is important to note that if intermediate mass ($4 - 8M_\odot$) AGB stars are the main source of enriched material from which the second generation forms, this event cannot start before $100 - 150Myr$ since the formation of the cluster. This is in contradiction with recent results on young clusters, with ages $< 100Myr$ where split MSa and eMSTO have been observed (Milone et al. 2015a, 2016, 2017).

1.2.3 Rotation-spread scenario

The *rotational* scenario was first introduced by (Bastian et al. 2009) as an alternative explanation for the split MS and eMSTO. This interpretation allows to describe the particular features observed in the CMD without accounting for a prolonged star formation. Instead, just one coeval population is needed and the split MS and eMSTO are the result of some effects due to the different stellar rotation rates.

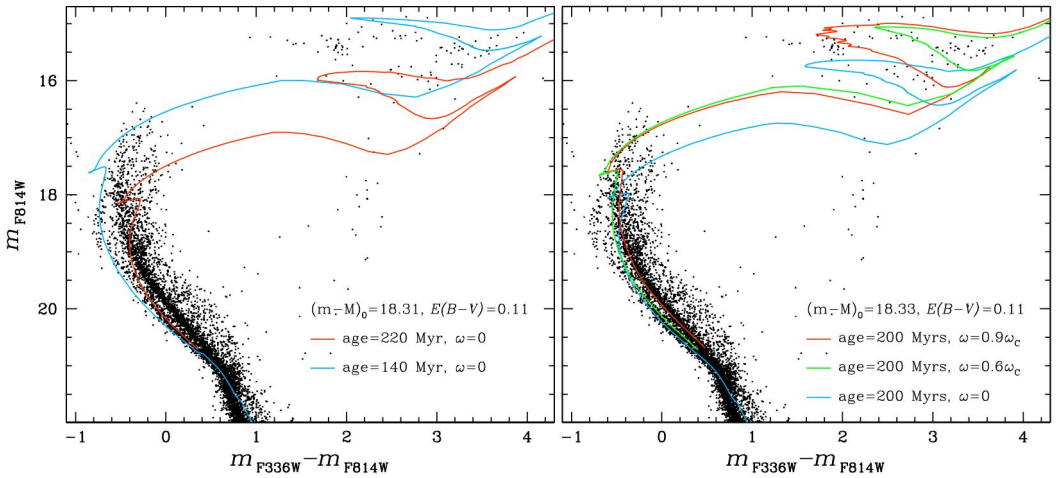

Figure 1.5: Comparison between the observed CMD of stars in NGC 1866 and isochrones. In the left-hand panel are plotted two non-rotating isochrones with different ages while in the right-hand panel three coeval isochrones with different rotations velocities of $\omega = 0$, $\omega = 0.6\omega_c$ and $\omega = 0.9\omega_c$ are shown. Figure taken from (Milone et al. 2016).

- A first consequence of stellar rotation is to reduce gravity at the surface, resulting in lower luminosities and effective temperatures.
- A second outcome is linked to the star orientation with respect to the line of sight. A high rotation rate deforms the star that tends to assume an oblate shape and thus develop a polar temperature gradient, appearing brighter and hotter if viewed pole-on.
- Finally, rotation can induce mixing processes that modify the composition of the envelope and the size of the stellar core, resulting in cooler temperatures and higher luminosities for turn-off stars.

As concluded by (Bastian et al. 2009) all the effects induced by rotation can substantially shape the CMDs of clusters even for moderate rotation rates, but strongly depend on the inclination angles distribution assumed between the stars and the observer. The variation of the separation in color between the blue and red sequences in different CMDs suggests that, at a fixed magnitude, bMS and rMS stars have different effective temperatures (Milone et al. 2016).
An important relation is the one reported by (Brandt et al. 2015) between the extension of the eMSTO and the cluster age: the first quantity is computed as the area enclosed by the rotating and non-rotating isochrones delimiting the eMSTO in units of mag^2: in figure 1.4 we can see that turn-off extensions are almost constant or somewhat increasing for cluster ages up to $1 - 1.6Gyr$, after whose age the extended turn-off rapidly disappears as a consequence of stars developing outer convective envelopes while still on the MS phase.

1.2.4 Disentangling between Age and Rotation

The age-spread and the rotation-spread hypothesis were strongly debated in the last years (e.g. Girardi et al. 2011). As we have seen a simple age-spread scenario is

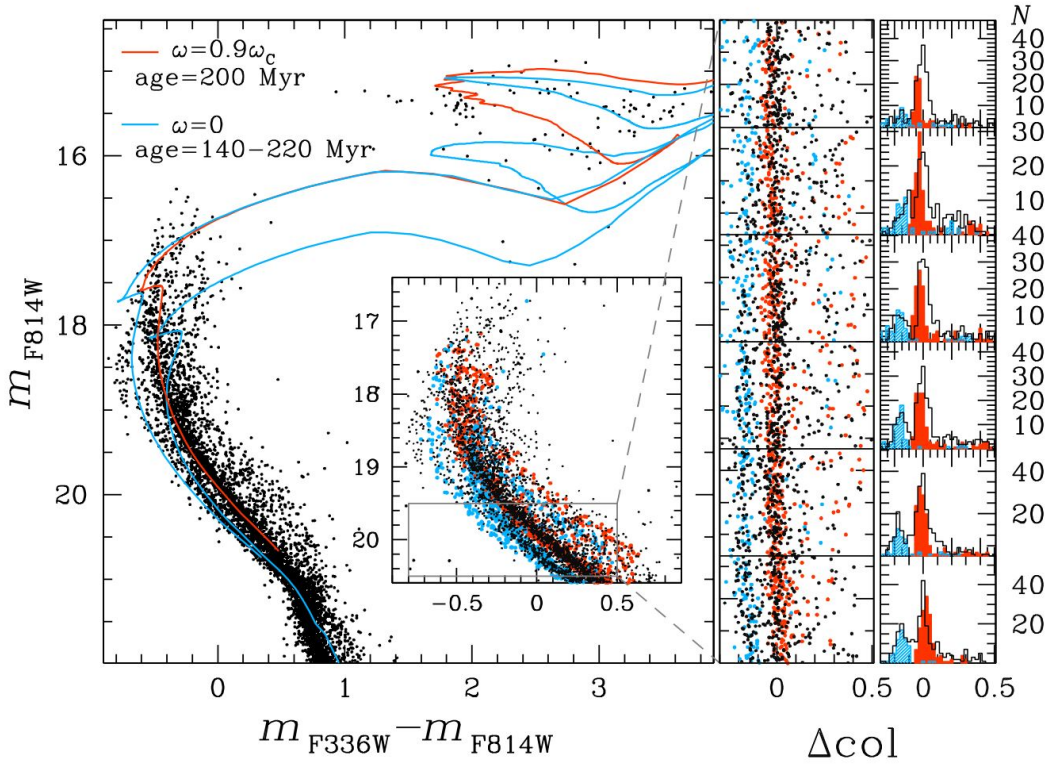

Figure 1.6: $m_{F336W} - m_{f814W}$ versus m_{F814W} CMD of NGC 1866 with three isochrones chosen to best reproduce the observed star distribution. The red isochrone is for a rapidly rotating population ($\omega = 0.9\omega_c$) of $200Myr$ of age while the two cyan isochrones are for non-rotating populations of $140Myr$ and $220Myr$. The inset shows the upper part of the MS and the simulated populations derived from the three isochrones. The middle panel shows the verticalized M_{F814W} vs Δcol distribution and the right-hand panel the Δcol histogram distributions in 5 magnitude intervals for the observed and simulated populations. Figure taken from (Milone et al. 2016).

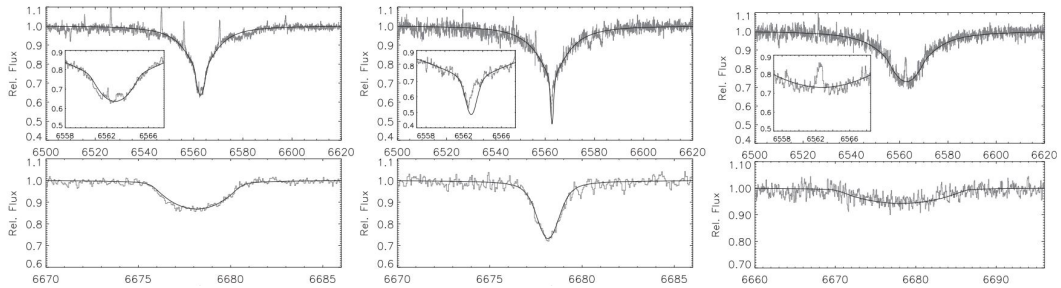

Figure 1.7: Observed and synthetic NLTE spectra around $H\alpha$ (top) and HeI (bottom) lines, for three stars belonging to the eMSTO (left panel), bMS (central panel) and rMS (right panel) of NGC 1818. Image taken from (Marino et al. 2018a). Note the narrower line profile for the bMS star with respect to the rMS star, indicating a lower projected rotational velocity for the former and a higher for the latter (computed to be $v\sin i = 29 \pm 2$ and $347 \pm 6\ km \cdot s^{-1}$, respectively.

not able to reproduce the split MS although it has been the most straightforward hypothesis to explain the eMSTO when this was first discovered in intermediate-age clusters. Its discovery, together with the discovery of the eMSTO and split MS in young clusters, has led to the formulation of the rotational scenario. However, this one alone still seems not sufficient to explain all features in young clusters' CMD. As well illustrated from the left-hand panel in figure 1.5 taken from (Milone et al. 2016), isochrones with an age-spread could in principle describe the extended turn-off region but barely reproduce the split MSs. On the other side, as illustrated from the right-hand panel in the same figure, coeval isochrones with different rotational velocities can describe in a satisfactory manner the split MSs but are not able to reproduce the eMSTO, particularly the upper part of the blue MS. The best model to reproduce all these features is obtained considering different rotation rates along with an age-spread. As an example, figure 1.6, taken from (Milone et al. 2016), shows a rapidly rotating isochrone (in red) with age og $200Myr$ and $\omega = 0.9\omega_c$ (where ω is the rotational velocity and ω_c is the break-up velocity) and two non-rotating isochrones (in blue) with ages of $140Myr$ and $220Myr$, where the first is needed to reproduce the upper part of the blue MS (or bluer part of the eMSTO). In the inset the upper MS and turn-off region of the CMD are shown together with simulated populations derived from the considered isochrones. The middle panel shows the verticalized M_{F814W} vs Δcol distribution and the right-hand panel the histogram Δcol distributions of the observed and simulated populations in 5 magnitude intervals.

1.3 Braking processes and binaries

In the last years the rotational scenario has been increasingly supported by new elements and is now the favourite scenario to explain the observed split MS. Nevertheless, some issues are unresolved and many other questions have risen: why are there two populations with different rotation velocities? are there actually fast rotators? But the principal query concerns the physical mechanism or mechanisms which lead to this separation in velocities. Were stars born with such rotation differences, or have they undergone some process which changed their velocities subsequently to their formation?

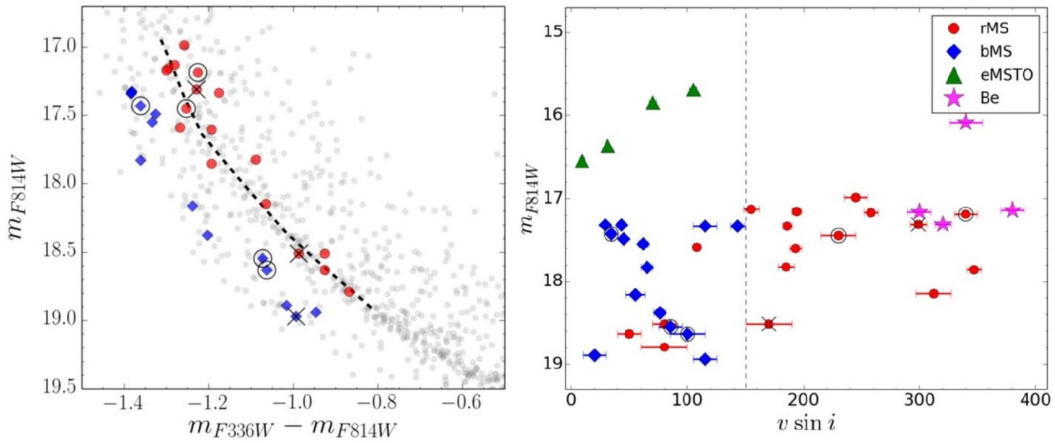

Figure 1.8: Left panel shows the CMD of NGC 1818 on the split MS region. Stars belonging to the bMS and rMS are highlighted in blue and red respectively. Right panel shows m_{F814W} magnitude as a function of $v\sin i$ $[km\,s^{-1}]$ projected velocity for NGC 1818 stars populating different region on the CMD including eMSTO and Be stars in addition to bMS and rMS stars from the left panel. Both figures are taken from (Marino et al. 2018a).

1.3.1 Evidence for stellar rotation

In following subsections are reported some considerations about the possible processes which affect stellar rotation and how they could be investigated from color-magnitude diagrams; but the strongest evidence to discriminate between fast and slow rotators would be to measure rotation velocities from spectral lines of both blue and red MS stars. Indeed this study has been conducted by (Marino et al. 2018a) analyzing the spectra of 44 stars in the rMS, bMS and eMSTO regions of the CMD of NGC 1818. Figure 1.7 shows the observed spectra of three different stars, compared with synthetic ones: it is evident that the central panel, referring to a star belonging to the blue MS, displays a narrower spectral line indicating a lower rotational velocity with respect to the two side panels, referring to stars belonging to the eMSTO (left) and red MS (right). Indeed, the effect of rotation on spectra is to broaden the line profile, if observed with sufficiently high spectral resolution.

A different approach that involves photometry concerns the position on the CMD of *Be* stars, which are $H\alpha$ emitters and are known to be very fast rotators, and thus should be confined to the red turn-off region. Abscissa of figure 1.8 taken from (Marino et al. 2018a) indicates the projected rotational velocity, which is a lower limit to the actual rotation rate, for stars from different regions in the CMD. It can be noted that *Be* stars are among those with the highest rotation velocities. Instead, bMS stars show low rotation velocities, while rMS stars span over a wider range of rotation rates, with an average higher value.
Left panel of figure 1.9 shows the $m_{F656N} - m_{F814W}$ versus m_{F336W} CMD of NGC 2164 from which the selection of *Be* stars (highlighted in magenta) is more straightforward, having a lower and wider range of colors than the thinner MS; right panel shows the $m_{F336W} - m_{F814W}$ versus m_{F336W} CMD in which *Be* stars clearly position themselves on the red part of the eMSTO.
According to (D'Antona et al. 2015) a possible source of information on stellar ro-

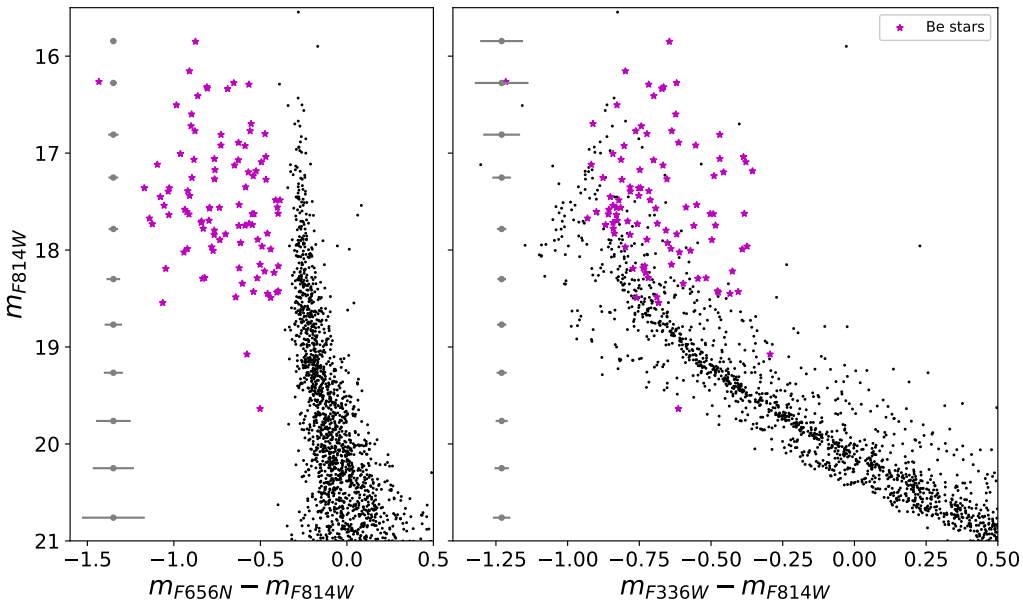

Figure 1.9: *Be* stars in NGC 2164 plotted in two different CMD combinations. In the $m_{F656N} - m_{F814W}$ versus m_{F336W} CMD the separation from the MS is most evident due to the H_α excess luminosity of those stars in the narrow-band filter $F656N$.

tation could come from studies on B- and A-type stars in the field, since these stars are mostly rapid rotators with velocities typical of the rMS stars.

1.3.2 Rotational evolution

With the expression *rotational evolution* we refer to the possibility that some stars were born with higher rotational velocities and have successively been slowed down losing their angular momentum. This hypothesis has been accurately studied by (D'Antona et al. 2017), showing how slow rotating stars are not younger in age, but only in a less advanced burning stage, thus appearing younger. The difference in time spent on the main sequence is mainly due to the internal mixing that bring new hydrogen-rich matter to the convective core, extending the lifetime of the star on the MS.

A test to discriminate between the evolutionary scenario and the two differently-born populations model could be provided by the study of the surface anomalies on CNO elements. As computed by (Ekström et al. 2012) the abundances of CNO and other elements measured from spectra of MS stars should be similar for both the blue and red sequences if the slow rotating stars have been braked from an initial fast rotating condition, but these abundances should differ if the stars belonging to the blue MS were born non rotating.
Actually in young and intermediate-age clusters we do not notice a high variability in those elements' abundances, in favour of the evolutionary scenario.

1.3.3 Braking mechanisms

Focusing on the braking scenario, what is the origin of the slowly rotating or non-rotating population? There are two main processes responsible for the braking of a star (D'Antona et al. 2017; Milone et al. 2016):

Magnetic Braking External layers may be the firsts to brake: the physical process responsible of slowing down these layers is the *magnetic wind braking*. The velocity variation then propagates toward the stellar interior by efficient angular momentum transport. According to (Zorec et al. 2012) stars can loose their angular momentum due to this effect still in the pre-MS phase and reach the main sequence already slowed down.

Tidal interactions Alternatively the core may be the first to brake due to tidal interaction in binary systems and subsequently the braking effect propagate outward to the stellar envelope, which will be the last layer to be slowed down.

Considering the second mechanism, for low mass stars with a convective envelope the braking is due to viscous dissipation of the kinetic energy, while for more massive stars with a convective core the braking is due to low-frequency oscillation modes excited by the periodic dynamical tide. From a study on A- and B-type binaries (Abt et al. 2004) it appears that close binaries with period between 4 and 500 days have a rotational velocity significantly smaller than single stars; very tight binaries with period shorter than 4 days are synchronized and wide binaries with period larger than 500 days show the rotational properties of single stars (this means that the braking mechanism produced by binary interactions is not efficient for wide binaries, characterized by larger orbital semi-axis).
Most of the tidal interaction takes place in the pre-MS phase and around the Zero Age Main Sequence (ZAMS), so that these systems will be already slowed down when binary dispersion may be relevant (D'Antona et al. 2015).

Assuming a uniform rotation to have a simplified model, the following expression for the synchronization time can be obtained (Zahn 1977):

$$\frac{1}{t_{sync}} = 5 \cdot 2^{5/3} (\frac{G\,M}{R^3})^{1/2} q^2 (1+q)^{5/6} \frac{M\,R^2}{I} E_2 (\frac{R}{a})^{17/2} \tag{1.1}$$

where $q = \frac{M_2}{M_1}$ is the mass ratio, E_2 is a parameter measuring the coupling between the tidal potential and the gravity mode which depends on the convective core mass. In most binary systems the momentum of inertia I of the stars is much smaller than the orbital momentum defined by $[q/(1+q)]Ma^2$ and the variation of the orbital velocity can be neglected with respect to the variation of the rotational velocity. Low-mass-ratio binaries usually have smaller separations and hence larger binding energies $E \propto qM^2/a$. A smaller binary separation produces in turn a stronger tidal interaction reducing the synchronization time-scale t_{sync} for primary stars in low-mass-ratio binary systems (Yang et al. 2018). As a result low-mass companions would make the binary system bluer than what would a high-mass companion do.

Considering the tidal torque effect as responsible for the slowing down of binary systems, stars will reach their final position on the non-rotating sequence only when braking of stellar rotation reaches the envelope and the photosphere. If this stage is reached before the end of the main sequence phase, the star will move to the blue main sequence, appearing younger and at the same time reducing its MS lifetime, because full braking may prevent further core-envelope mixing.

The two main effects of this mechanism are the appearance of a younger blue MS and the presence of older stars in the extended turn off.

1.4 Thesis layout

In this work I exploit photometric data obtained with the *Hubble Space Telescope* for the young LMC cluster NGC 2164 to focus on the split Main Sequence. The aim of this thesis is to characterize the binary systems distribution along the two MSs and constrain, for the first time, the frequency of binaries among multiple populations. A prevalence of binaries belonging to the blue MS would corroborate the connection between binaries and split MSs in young clusters. This result would also uphold the hypothesis of binary interactions as an efficient braking mechanism of stellar rotation, as proposed in previous sections.

In chapter 2 I present the dataset obtained from HST observations and the reduction and calibration that has been followed.

In chapter 3 I present some previous results on NGC 2164 from literature and then the Color Magnitude Diagrams (CMDs) investigated in this work, motivating the choice of the combination of filters adopted. At the end of this chapter I also present a new feature observed in these CMDs, characterizing the upper part of the MS.

In chapter 4 I show in detail the adopted procedure to investigate the main question addressed by this study. In the first part of this chapter, I present the theoretical insight behind this approach and focus on the observational data to select and derive the distribution of binaries. In the second part of this chapter I make use of artificial stars simulation analysis to infer the binary systems properties that are the object of interest of this work.

Finally, in chapter 5 I summarize the obtained results and discuss them.

CHAPTER 2

HST observation and data reduction

The foregoing thought that old globular clusters and, in more recent years, young clusters could be considered as SSPs had been challenged and eventually disproved by more recent observations. Specially relevant to the new understanding of star clusters have been the high resolution images and large wavelength-band data provided by space observations, being not affected by the presence of the atmosphere. Indeed, atmosphere introduces turbulence effects (i.e. seeing), and limits the wavelength windows preventing observation in the ultra-violet range of the electromagnetic spectra below $\lambda = 400nm$. To acquire data in this wavelength region, space observations are mandatory. Furthermore, to investigate, as is the aim of this thesis, a physical process that shows itself as a fine feature on the CMD of young clusters, the best photometry available to date is necessary.

Instrumentation The multi-band images from which the photometry of NGC 2164 has been obtained were collected through the Ultraviolet and Visual (UVIS) channel of the Wide-Field Camera 3 (WFC3) on board HST. WFC3 has been installed on HST servicing mission 4 in May 2009 replacing the previous WFPC2.
WFC3, with its two UVIS and IR channel combined, is capable of high resolution imaging in the entire wavelenght range from the ultra-violet $\lambda = 200nm$ to the near infra-red $\lambda = 1700nm$. The UVIS channel here exploited operate on a wavelenght range going from $\lambda = 200nm$ to $\lambda = 1000nm$ using a combination of wide, intermediate and narrow-band filters.

2.1 HST data

The dataset used in this thesis has been collected as part of the programs GO 13727 and 14710 with J. Kalirai and A. P. Milone as principal investigator, respectively. n Images were obtained in the three $F225W$, $F336W$ and $F814W$ wide-band filters and in the $F656N$ narrow-band filter; in figure 2.1 I show the four stacked images, one for each filter, obtained by the reduction procedure described in the following section. I summarize in table 2.1 the dataset used for this study, complete of acquisition dates and exposure times.
In figure 2.3 I show the trichromatic stacked image of NGC 2164 obtained through

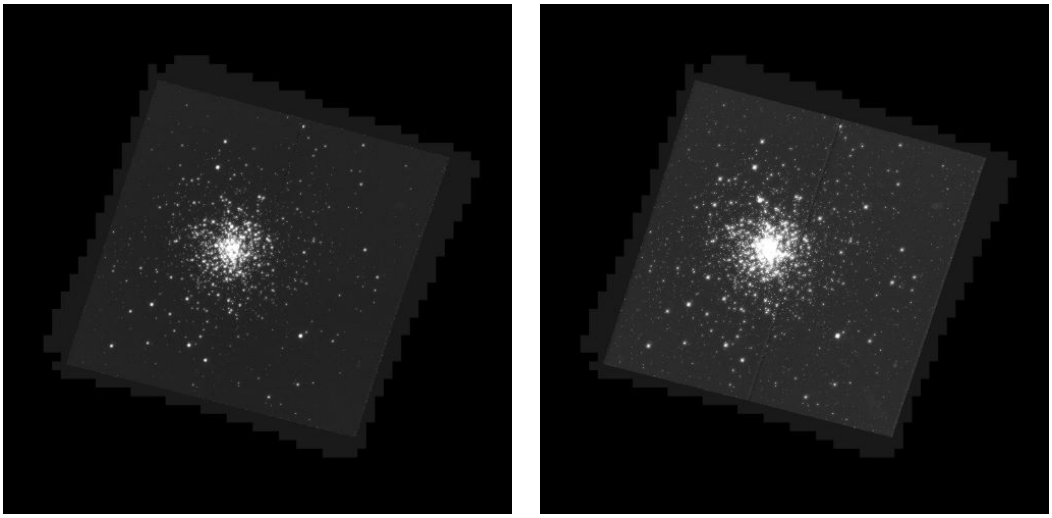

(a) F225W

(b) F336W

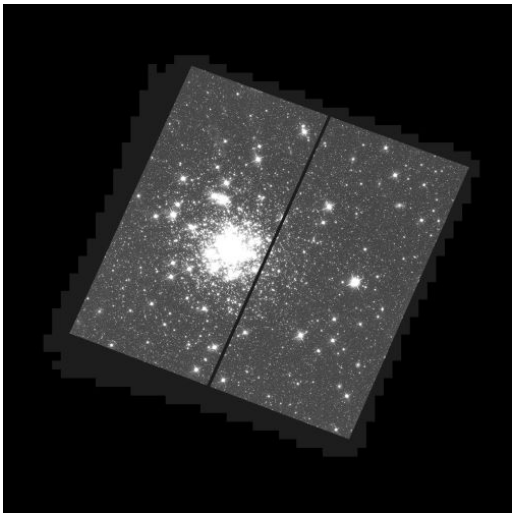

(c) F814W

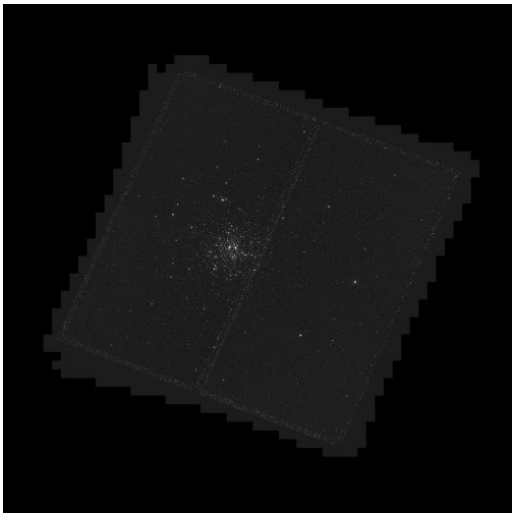

(d) F656N

Figure 2.1: Stacked images obtained from different filters.

the three wide-band filters $F225W$, $F336W$ and $F814W$ and making use of the *SAOimageDS9* imaging software. Circles superimposed on this image delimit the cluster and the reference field regions, as better described in section 3.2.

2.2 Reduction

Stellar astrometry and photometry have been carried out using the images corrected for bias and flat-field effects, using the procedure and the computer programs developed (Anderson et al. 2008) and references therein.
The first step consists in removing the effect of poor charge-transfer efficiency (CTE) by using an empirical pixel-based method (Anderson et al. 2010) that reproduces the trails observed in a large sample of analyzed dark exposures. The software then converts these trails into an estimate of the original pixel value by inverting the derived model. The data reduction is based on Point-Spread Function (PSF) photometry.

date	camera	filter	exposure time	GO
2015, Sep, 5	UVIS/WFC3	F225W	4800s (10s+100s+5x938s)	13727
2015, Sep, 5-6	UVIS/WFC3	F336W	3741s (10s+100s+790s+3x947s)	13727
2017, Feb, 27	UVIS/WFC3	F656N	1440s (2x720s)	14710
2017, Feb, 27	UVIS/WFC3	F814W	808s (90s+758s)	14710

Table 2.1: HST observational dataset.

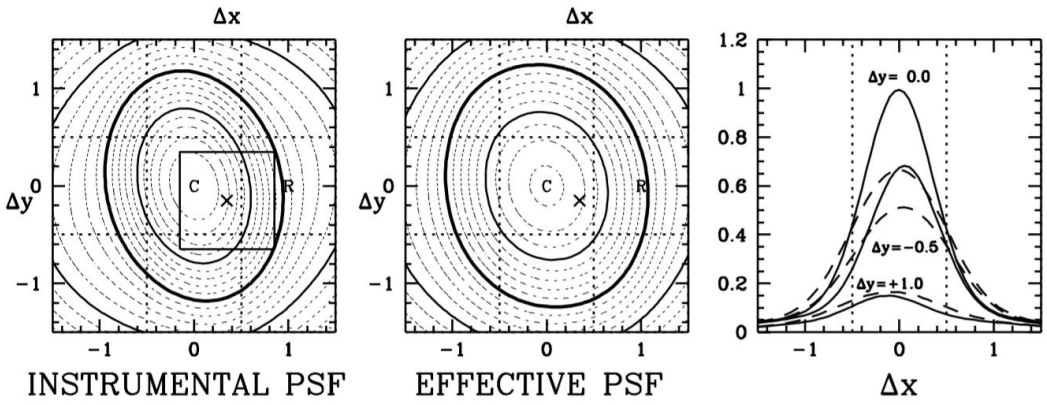

Figure 2.2: Instrumental and effective PSF models. Figure taken from (Anderson et al. 2000).

2.2.1 Effective PSF

Astrometric and photometric data of point sources are determined by only three parameters: the position of the source (x,y) and its flux (f). This information is extracted from the array of pixels that constitute the image of the star on the detector by means of its PSF.
In Charge Coupled Devices (CCD) the PSF is given by the convolution of two functions that unfortunately are not directly observable. The first is the instrumental PSF (iPSF) which gives the flux for a point source as a function of offset from its center, and the second is the pixel response function that gives the sensitivity at each point in the pixel. To bypass this limit the data have been reduced using an approach developed by (Anderson et al. 2000) based on the effective PSF (ePSF), which is a continuous function of the offset form the center of the PSF (Δx,Δy) whose value is the fraction of light of a point source that would fall in a pixel centered at that point. An example of iPSF and ePSF is shown in figure 2.2 taken from (Anderson et al. 2000).

The determination of the precise PSF can stumble across some issues, as for example the fact that HST observations, being not affected by atmosphere effects, have a Full Width at Half Maximum (FWHM) of its iPSF that cover just 2-3 pixels and that is for that reason under-sampled. This effect leads to some degeneracy problems in determining the exact position of the PSF center, but can be overcome by applying a *dithering* technique to the image acquisition procedure: this consist in shifting by a very small amount the Field of View (FoV) from one observation to

another, so that a point source does not fall on the same pixels every time.
Another relevant issue in the ePSF determination is that its shape can change with location on the detector. To derive the most precise information, instead of a single PSF model a grid of PSFs is created and each source is reduced by interpolating its PSF with the nearest four in the model grid. Finally, to account also for a small temporal variability of the PSF core, due to an effect of focus changing with time called "breathing" the PSF model is constructed as a sum of a library PSF and small perturbation PSF, built from the residuals of the fit of the star flux with the library PSF.
A most accurate PSF model determination is requested to extract high precision data from each image. The PSF models are derived in each image using the *img2psf* routine (Anderson et al. 2000) exploiting only isolated, bright and non saturated stars. This routine takes in input a number of parameters (e.g. isolation index, minimum and maximum flux, maximum Q-fit, number of regions, initial PSF guess and the image to analyze) anderson2008 milone2009

2.2.2 Catalog building

Having derived the PSF models, this can now be applied to determine the position and magnitude of every star, also the fainter ones that were not considered in the previous steps.
Two different approaches are considered:

- For bright stars, the ePSF reduction is run on each exposure singularly and the results are then combined together.
- For faint stars the ePSF reduction is applied to the stacked image obtained as the sum of every exposure in the same filter.

The second method increase the Signal-to-Noise ratio (S/N), important aspect at faint magnitudes, but worsen the accuracy for bright stars. For that reason both approaches have been considered.

For brighter stars the reduction is worked by the *img2xym* routine (Anderson et al. 2006) that gives as outputs the x any y coordinates of the stars in the reference frame of the image, the magnitude in instrumental units, that is $mag = -2.5log(flux)$ where the flux is expressed in photo-electrons counts in the reference exposure, and the *q-fit* value that is indicative of the quality of the fit between the observed star and the best-model PSF.

At this point of the procedure we are left with one catalog for every image, each one with its reference frame. Next step is then necessary to find the right coordinate transformation from one to another, creating thus a single reference catalog.
In order to do this has been exploited a set of fortran routines by Jay Anderson: namely *xym2mat*, *xym2bar* and *xym1mat*. The first program performs the task to find the parameter of the linear transformation between a set of input catalogs and a reference one, and then corrects them for geometrical distortion, according to the selected filter and CCD's chip. At this point *xym2bar* generates one single catalog for each filter available in which the magnitude of a star is computed as the mean magnitude derived from the different exposures. In order to account for the exposure time this part has been slightly modified to weigh the final mean magnitude with the exposure time. This leads to a better estimate of the magnitude, since it does not mix long exposure images with short ones. As a final step *xym1mat* links the

catalogs in different filters, creating the final astro-photometric catalog.

The procedure followed for fainter stars that exploits stacked images is made through the *KS2.F* routine by (Anderson et al. 2008).
Using the stacked images produced by this routine I also created the RGB image of the field of view shown in figure 2.3.

2.3 Calibration

The last step is needed to calibrate the instrumental magnitudes m_{inst}. Calibrated magnitudes m_{cal} are obtained as

$$m_{cal} = m_{inst} + \Delta mag + ZP_{filter} + C \tag{2.1}$$

where Δmag is the difference between the PSF magnitude and the aperture photometry magnitude, ZP is the zero point correction for a given filter and C is the aperture correction. The zero point and the aperture correction parameters have been taken from http://www.stsci.edu/hst/acs/analysis/zeropoints, considering the date of observation, the filter used and the selected aperture radius. The aperture photometry measures the flux of the star included in an area within a radius computed to be the largest possible without introducing contamination from surrounding stars, and the ideal radius is estimated considering the aperture radius and a sky annular region around the star to compare the dispersion of Δmag for different values of these radii through the *drz_phot_gfortran.F* routine by Jay Anderson.

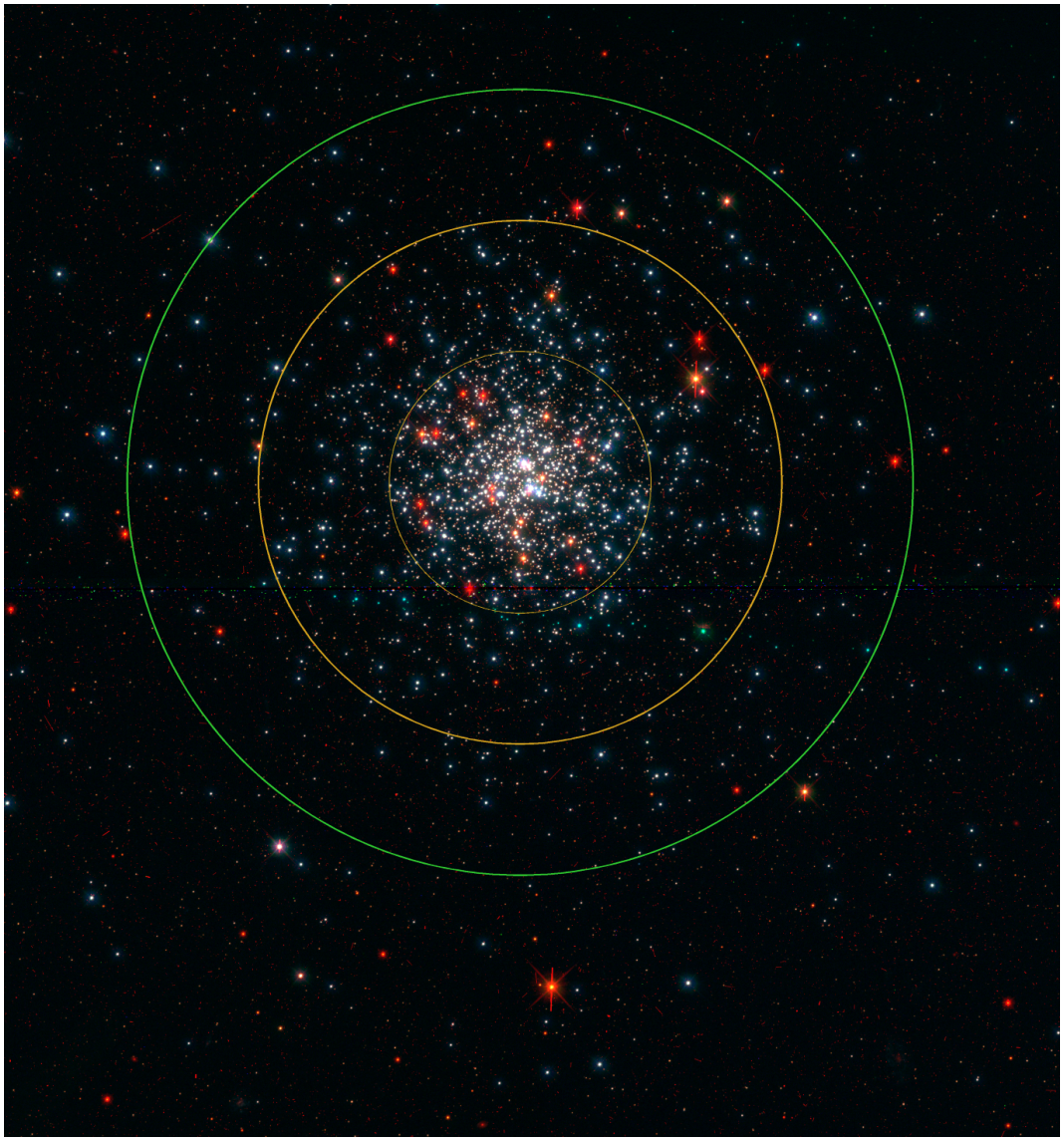

Figure 2.3: Tri-color image of NGC 2164 obtained by combining F225W, F336W and F814W stacked images. The golden thin circle marks the half-light radius of the cluster, $r_{hl} = 18$". Golden thick circle delimits the defined cluster region within twice the half-light radius, and green circle is the internal limit of the reference field, at three times r_{hl}. Colors have been chosen to be consistent with cluster and reference field throughout all figures of the thesis.

CHAPTER 3

CMD of NGC 2164

3.1 Literature studies on NGC 2164

NGC 2164 is a ∼100-Myr old cluster in the Large Magellanic Cloud (see Table 3.1 for the main structure parameters). Its mass of $\sim 1.5 \times 10^4 M_\odot$, is smaller than the mass threshold ($\sim 6 \times 10^4 M_\odot$) proposed by (Goudfrooij et al. 2014) as a lower limit for a cluster to retain the ejecta from AGB stars and thus forming the second generation. The reddening is almost constant across the *HST* field of view, as demonstrated by (Milone et al. 2018), who derived high-resolution reddening map around NGC 2164 and found that any variation of reddening, if present, should be smaller than E(B−V)∼0.003 mag. Since the possible amount of differential reddening is smaller than the typical observational uncertainty bright stars, our analysis is based on the magnitudes non-corrected for differential reddening.

Figure 3.1, (from Milone et al. 2018) compares three isochrones with the $m_{F336W} - m_{F814W}$ versus m_{F814W} CMD of NGC 2164. Specifically, the red isochrone corresponds to a rapidly-rotating population, with a rotation rate near the break-up limit and an age of 100 Myr. The blue isochrones superimposed on the bright and the faint MSTO are non-rotating stellar populations with ages of $80 Myr$ and $100 Myr$, respectively. The metallicity and the distance modulus inferred from the best-fit isochrones are quoted in the figure. Note that as discussed in section 1.2.4, internal age variation, together to a spread of stellar rotation rates are necessary to reproduce the split MS and the eMSTO of NGC 2164.

3.2 Cluster and reference field

On figure 2.3 I highlight with the golden and green thicker circles the external limit to the cluster region and the internal limit to the field reference frame respectively. The golden thinner internal circle represents the half-light radius of NGC 2164 ($r_{hl} = 4.37 pc$ from (McLaughlin et al. 2005)).

To derive the boundaries of the cluster and of the reference field (gold and green regions in Figure 3.2), I exploit the distribution of stars in the field of view.

The black dots plotted in the right panel show the stellar density (in star counts per $arcsec^2$ units) as a function of the distance from the cluster center, calculated

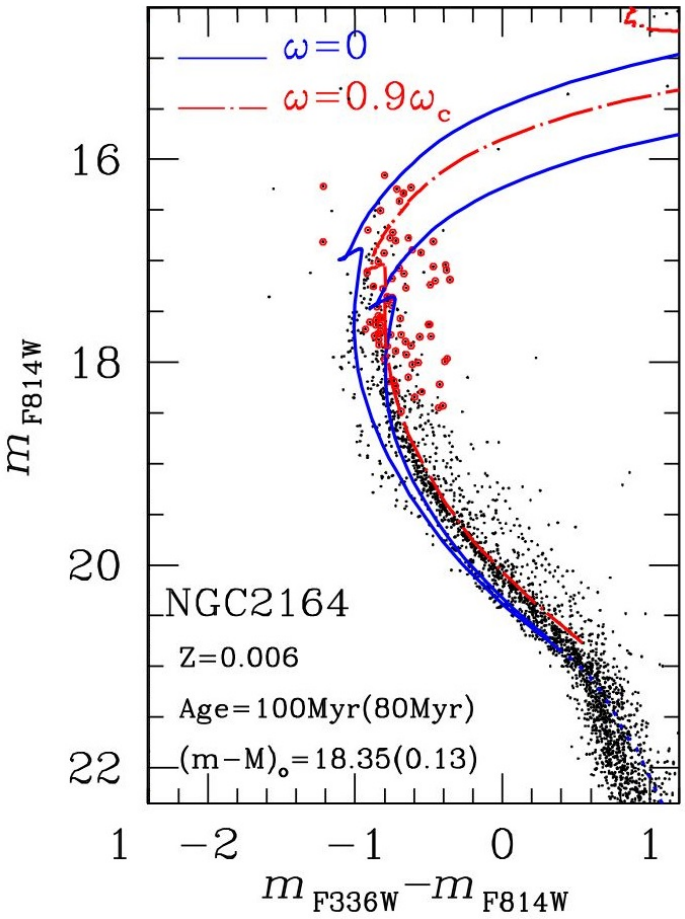

Figure 3.1: $m_{F336W} - m_{F814W}$ versus m_{F814W} CMD of NGC 2164 and isochrones with different ages and rotational velocities: in red for a rapidly rotating population of $100Myr$, in blue for non-rotating populations of $80Myr$ and $100Myr$. Figure taken from (Milone et al. 2018).

over concentric rings of 4 arc seconds width. The golden dotted line marks the half-light radius, $r_{hl} = 18$", whereas the golden-dashed line corresponds to a radial distance of two half-light radii and has been chosen as the radius of the cluster field. This choice is based on the fact that the majority of cluster members are located in the cluster region, as illustrated by the black line.

The green dashed line has been selected as the internal radius for the reference field and corresponds to three times the half-light radius. Clearly, the distribution of stars in the reference field is almost constant, thus suggesting negligible contamination from cluster members.

With a continuous blue (red) line I also plot the trend of the density of blue (red) MS stars inside the cluster region. I select stars in the F814W magnitude interval between 18.0 and 21.0 mag, where the two sequences are clearly separated. Noticeably, the blue MS is less populous than the red MS. Nevertheless, the population ratio depends on radial distance and the fraction of blue MS stars over red MS stars increases towards the cluster outskirts (purple dotted line, with its scale on the right side of the figure).

In figure 3.3 I present the Hess diagrams for the cluster and the reference filed.

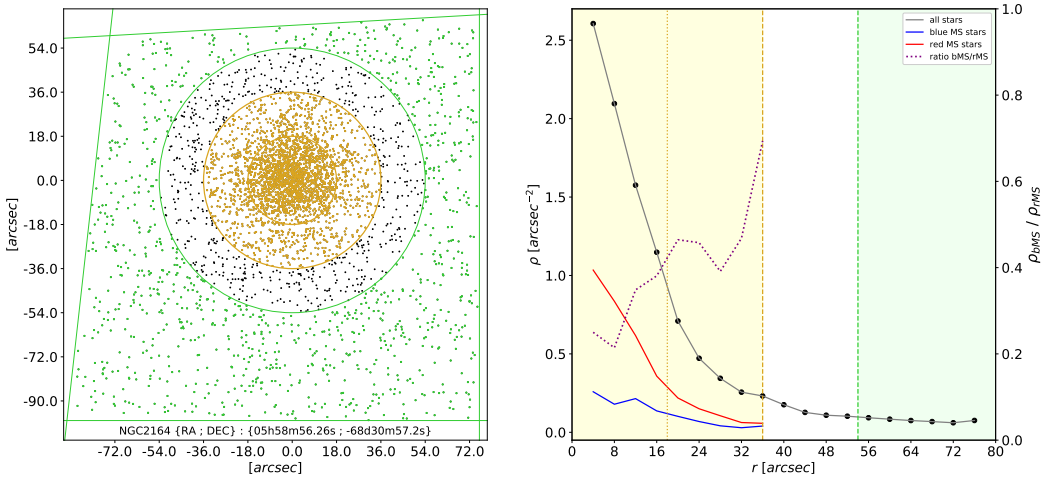

Figure 3.2: Left panel: Positions of all stars with high-quality photometry in the F225W, F336W and F814W bands. The golden and grey circle mark the cluster and reference field, respectively. Right panel: radial distribution of various groups. Dotted golden vertical line marks the half-light radius of 18 arcsec; golden and green dashed vertical lines are twice and three time its value respectively (taken as the cluster external limit and field region internal limit). Blue (red) continuous line shows the radial density distribution of blue (red) main sequence stars with $18.0 < m_{F814W} < 21.0$; the purple dotted line shows the ratio $\frac{bMS}{rMS}$ and its relative scale is on right side of the image.

Object	NGC 2164	source
RA (J2000)	05h 58m 56.26s	[1]
DEC (J2000)	-68° 30' 57.2"	[1]
Age	$100 Myr$	[2]
$log(\frac{M}{M_\odot})$	4.18	[3]
r_{hl}	$4.37 pc$	[3]
$(m-M)_0$	18.5	[4]
$E(B-V)$	0.13	[2]
Z (LMC)	0.006	[2]

Table 3.1: NGC 2164 parameters. [1] from https://ned.ipac.caltech.edu/; [2] from (Milone et al. 2018); [3] from (McLaughlin et al. 2005) assuming a Wilson profile; [4] LMC distance modulus

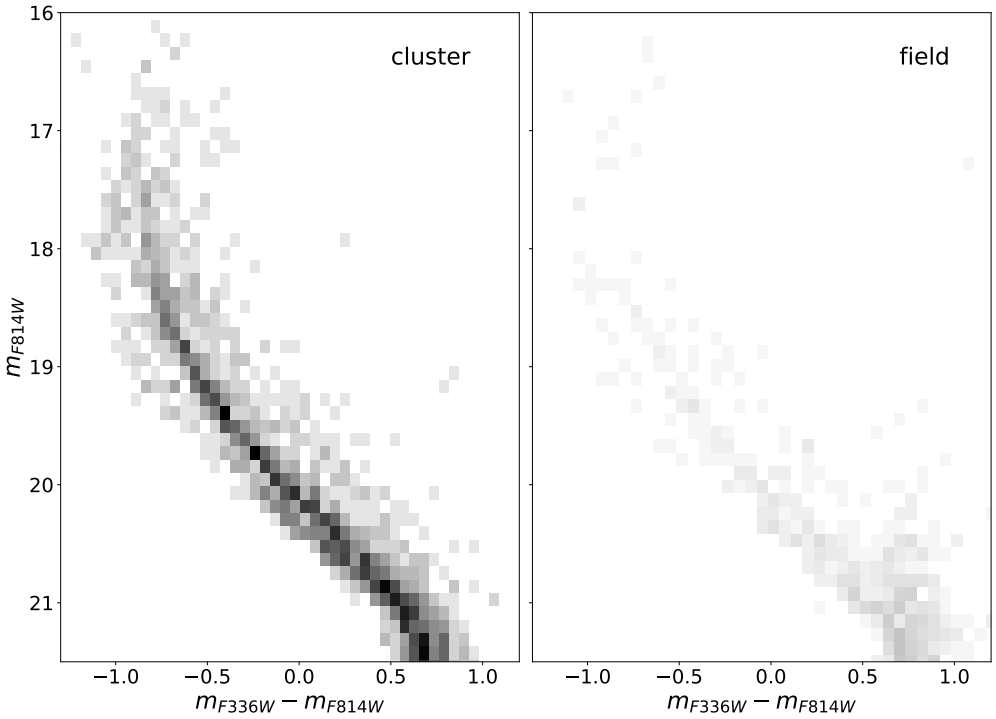

Figure 3.3: m_{F814W} vs. $m_{F336W} - m_{F814W}$ Hess diagrams of stars in the cluster (left) and reference field (right). I adopted the same scale for both diagrams.

Intriguingly, a hint of split MS is visible in the Hess diagram of field stars too. This feature of the CMD is consistent with a scenario where the split MS is not a peculiarity of cluster stars but is also present in the field. Indeed Milone2018 found no correlation between the cluster masses and the presence of an eMSTO in all the studied range of masses. Although spectroscopic investigation is mandatory to test this hypothesis, it is worth noting that the split MS have been observed in clusters that span a wide range of masses, thus suggesting that the environment does not play a major role in the formation of the split MS. Residual contamination from cluster members could also contribute to the apparent split MS in the reference field.

3.3 Filters choice

I present in this section a preliminary analysis of the different CMDs obtained for NGC 2164 with different combinations of filters among those available. In figure 3.4 I plot all the different CMDs obtainable with the three wide-band filters combining them to different colors. I choose to use the $m_{F336W} - m_{F814W}$ versus m_{F814W} CMD in panel (i) to separate the two MSs and the $m_{F225W} - m_{F336W}$ versus m_{F336W} CMD in panel (d) as the one from which to select the binaries to analyze. These two CMDs are better shown in figure 4.3 with the corresponding photometric errors indicated.
Photometric error calculation for these CMDs is shown in figure 3.6; the color uncertainties (lower panels) are obtained from the quadrature of the uncertainties from the single filters. σ_{F225W}, σ_{F336W} and σ_{F656N} are given by the relation $\sigma = \frac{rms}{\sqrt{N-1}}$ where rms indicates the "random mean scatter" and N is the number of exposures in which a star has been successfully detected. Since the rms quantity is not well determined with the $F814W$ filter, from consideration on artificial stars errors I choose to use a linear relation with $\sigma_{F814W} = 0.01$ at $m_{F814W} = 18.0$ and $\sigma_{F814W} = 0.015$ at $m_{F814W} = 21.0$ instead (panel b).

I show in figure 3.5 some CMDs obtained considering also the narrow-band filter $F656N$, and I highlight in magenta *Be* stars (see section 1.3)

3.4 Population ratio

I report in this sections a result from (Milone et al. 2018) that is of great relevance for the analysis I conduct in chapter 4. Observing the $m_{F336W} - m_{F814W}$ versus m_{F814W} CMD it clearly manifests that the two sequences in which the MS is split are not equally populated and the ratio $R_{MS} = \frac{N_{rMS}}{N_{bMS}}$ of blue MS stars over red MS stars does not keep constant with magnitude. It is fundamental to consider this parameter while determining the relative fraction of binaries belonging to each population.
I explain here the procedure that has been used to derive this ratio: it is based on the analysis of the $m_{F336W} - m_{F814W}$ versus m_{F814W} CMD and is illustrated in figure 3.7. The CMD has been analysed in the region where the split MS is more evident; the fiducial line of the red MS has been derived and used to verticalize the diagram, as shown in panel (c) in which the quantity Δcol is the difference between the $m_{F336W} - m_{F814W}$ color of the star and the $m_{F336W} - m_{F814W}$ color of the red

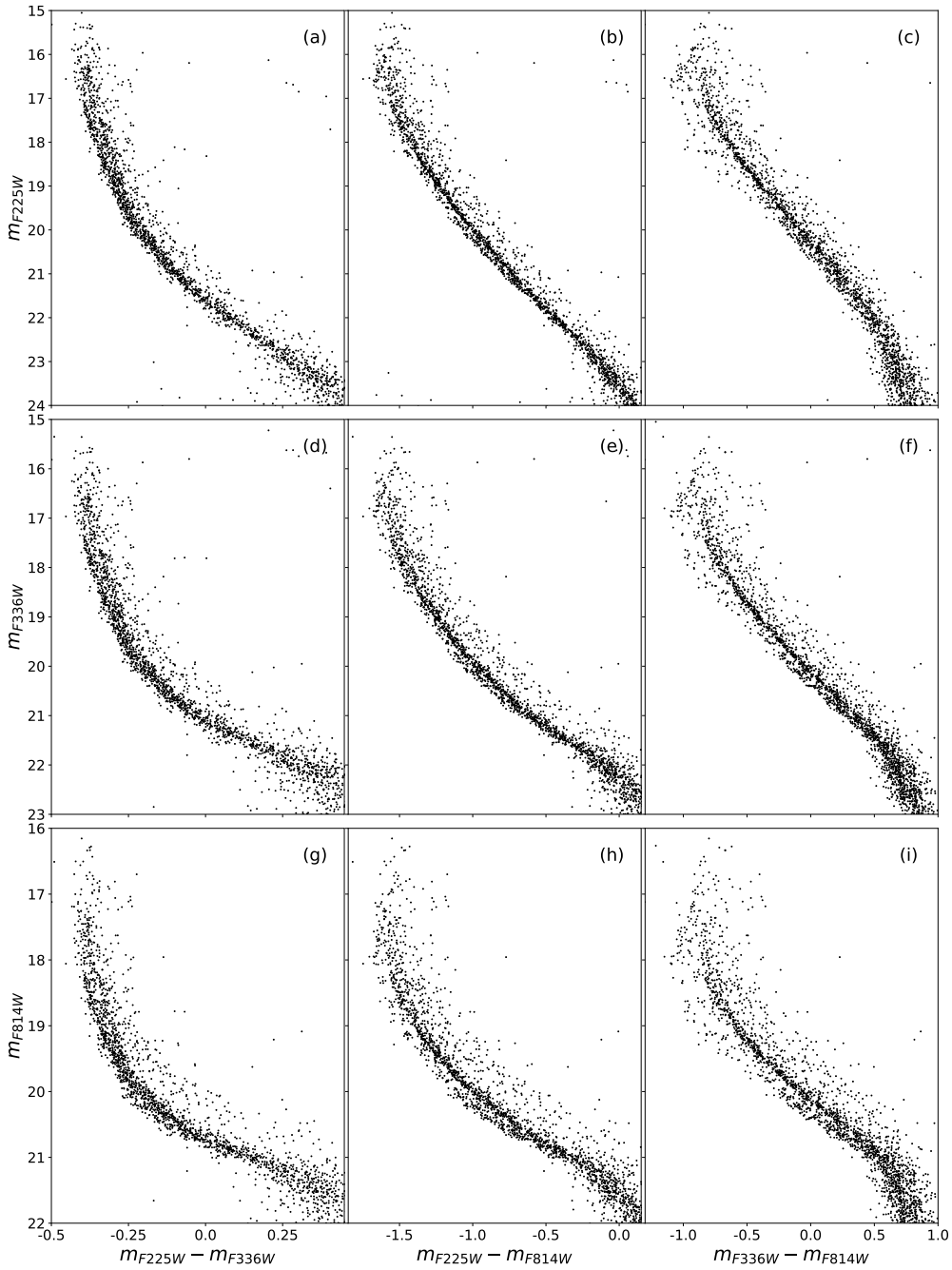

Figure 3.4: Collection of Color-Magnitude Diagrams of NGC 2164 obtained with the three wide-band filters F225W, F336W and F814W.

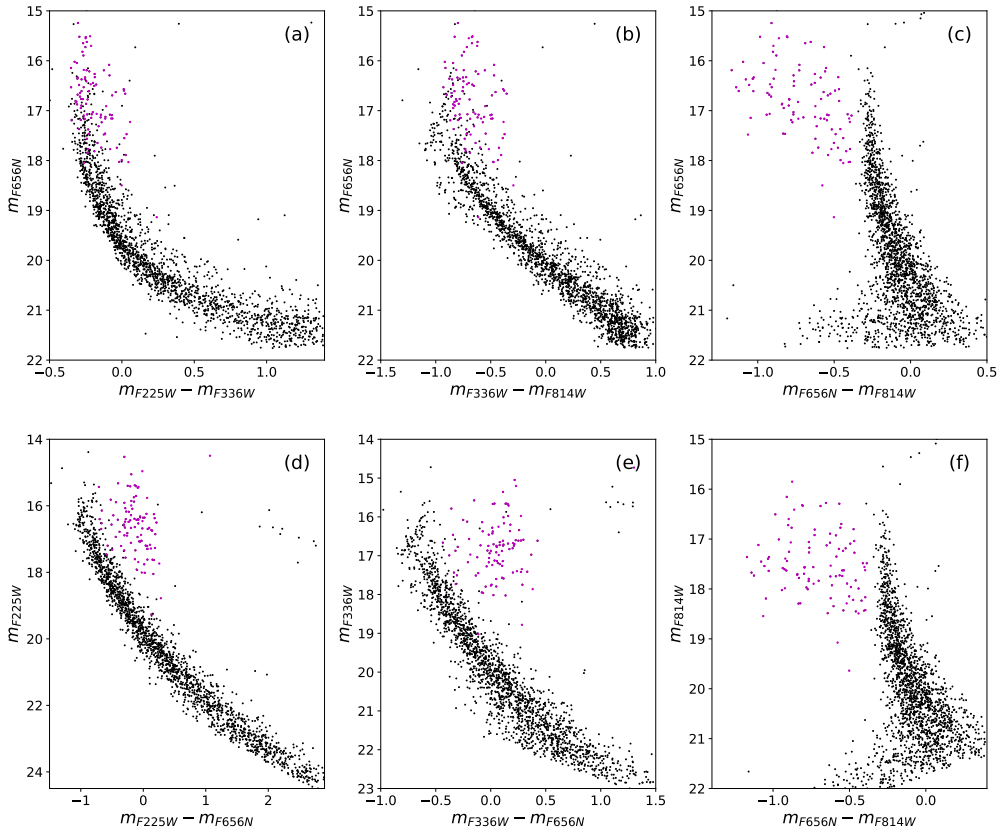

Figure 3.5: Color-Magnitude Diagrams of NGC 2164 that involve also the narrow-band filter F656N. Be stars are highlighted in magenta.

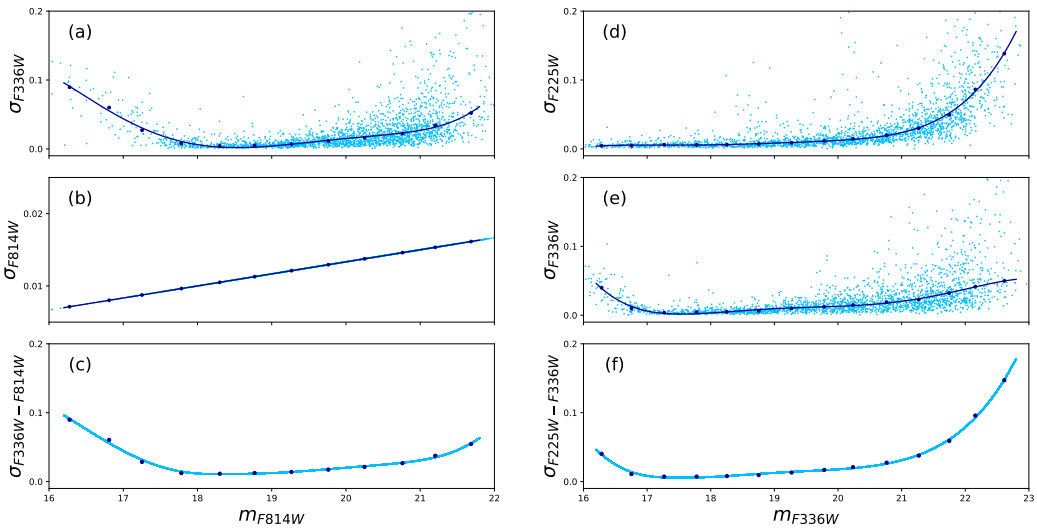

Figure 3.6: Estimate of photometric uncertainties for the magnitudes and colors used in this paper. Upper and middle panels show the *rms* of each filters against the magnitude while lower panes represent the color uncertainties.

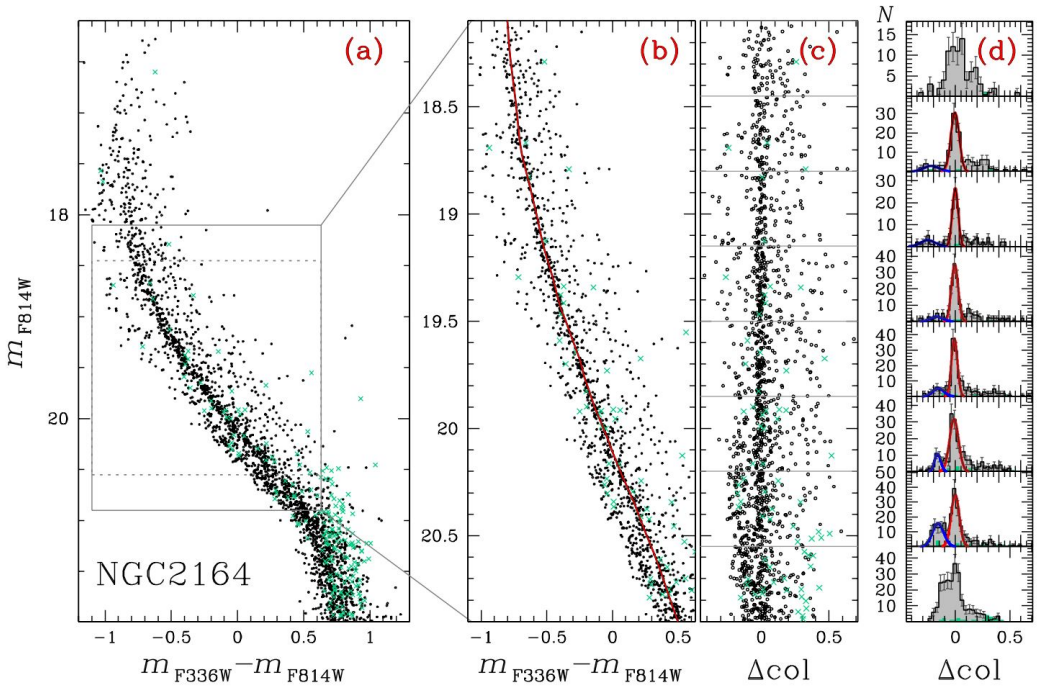

Figure 3.7: Illustration of the procedure to calculate the ratio between the blue MS and red MS populations. Taken from (Milone et al. 2018).

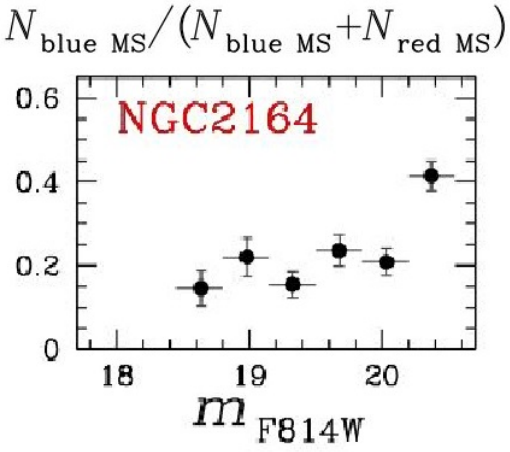

Figure 3.8: Fraction of blue-MS stars as a funcrion of cluster luminosity as derived from the procedure illustrated in figure 3.7 and described in text. Taken from (Milone et al. 2018).

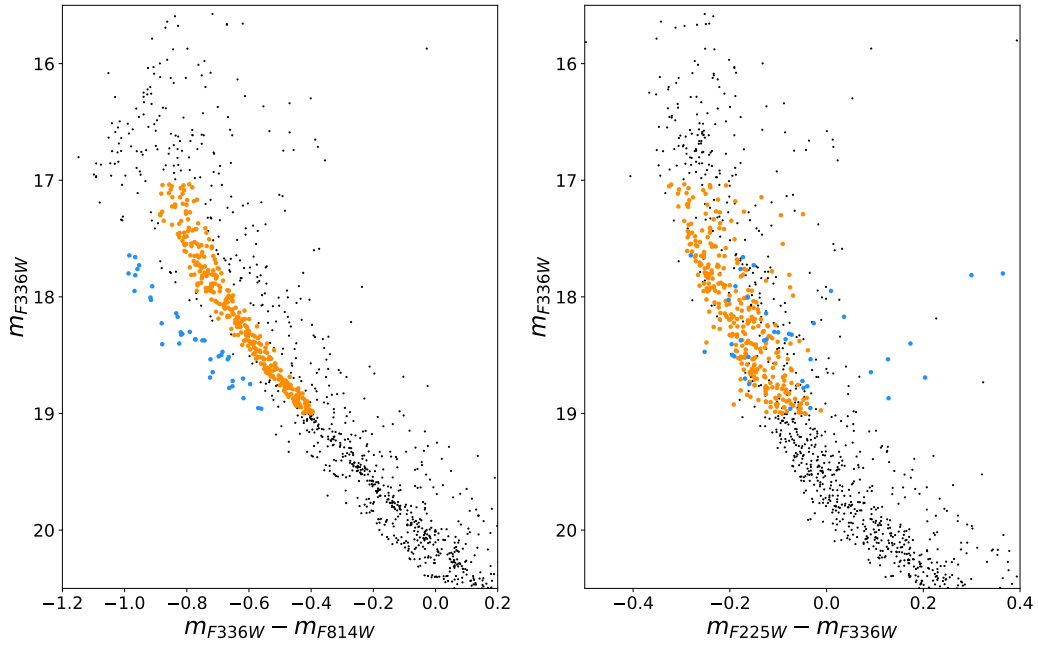

Figure 3.9: $m_{F336W} - m_{F814W}$ versus m_{F336W} CMD (left) and $m_{F225W} - m_{F336W}$ versus m_{F336W} CMD (right). The two groups of blue and red-MS stars selected in the left-panel CMD, are represented in azure and orange, respectively.

MS fiducial line at the same m_{F814W} magnitude. Successively 8 magnitude intervals of 0.35 mag each have been defined, and the relative histogram distributions are plotted in panel (d). These histograms highlight the bimodal distribution for most of the intervals, and a bi-Gaussian function has been applied to fit the distribution (excluding stars with $\Delta col > 0.08$ to minimize the effect of binaries) for all intervals except the lower and higher histograms: these have been excluded as for the former the split MSs merge together around $m_{F814W} = 20.8$, and for the latter stars begin to evolve from the MS. The ratio between the two populations is defined by the area under the two components of the bi-Gaussian fit. Results from this procedure are reported in figure 3.8, which is an inset from a larger figure in (Milone et al. 2018) including other clusters; in the case of NGC 2164 the ratio between blue MS stars and all MS stars is quite constant down to $m_{F814W} = 20$, at which level the contribution from blue MS stars begins to be more relevant. In my study over binaries distribution I have limited the selection region between $m_{F814W} = 18.5$ and $m_{F814W} = 19.75$: considering only this magnitudes interval in figure 3.8, I esteem a constant value of $\frac{N_{bMS}}{N_{bMS}+N_{rMS}} = 0.2$ which gives $R_{MS} = 4$.

3.5 A new feature in the upper MS: The triple sequence of NGC 2164

I present in this section a new intriguing feature that manifests from the analysis of multi-band photometry of NGC 2164. The upper red MS is narrow and well defined in the $m_{F336W} - m_{F814W}$ versus m_{F336W} CMD (panel (f) in Figure 3.4). Instead, red MS stars span a wide color range when I plot m_{F336W} against $m_{F225W} - m_{F336W}$.

This fact is illustrated in Figure 3.9. I select by eye the sample of blue-MS and red-MS stars from the left-panel CMD in the magnitude interval between $m_{F336W} = 17.0$ and $m_{F336W} = 19.0$. Then, I use the same colors to plot the selected stars in the m_{F336W} versus $m_{F225W} - m_{F336W}$ CMD. Clearly, red-MS stars define a broad sequence and exhibit hints of bimodal color distribution. This fact demonstrates that the red MS is not consistent with a single isochrone.

The color splitting of the upper MS in the $m_{F225W} - m_{F336W}$ versus m_{F336W} CMD (panel (d) in Figure 3.4) is further investigated in Figure 3.10. I select two sequences from the upper-left CMD and represent them with yellow and magenta colors. Moreover, I use green color to mark candidate binary systems. I use the same color codes to represent these stars in the $m_{F336W} - m_{F814W}$ versus m_{F336W} CMD (upper-right panel) and in the verticalized $\Delta C_{F225W-F336W}$ versus m_{F336W} and $\Delta C_{F336W-F814W}$ versus m_{F336W} diagrams that I plot in the middle panels. The verticalized diagrams are derived by using the fiducial lines of the yellow population (orange fiducial).

In the lower panels the histogram distributions are shown. It clearly appears that the two populations, which on the left panels are separated by construction, in the right panels strongly modify their distribution. The yellow sample is more concentrate while the magenta sample form a wider distribution toward redder colors, with the peculiarity of a second small peak at lower ΔC verticalized colors. These results corroborate the evidence that the red MS host at least two sub-populations of stars. It is particularly intriguing that the upper red MS is narrower in the CMD in which the split of the MS is wider, while in the CMD in which the lower MSs are blended the upper part is wider. More analysis are needed to confirm this feature and investigate its origin.

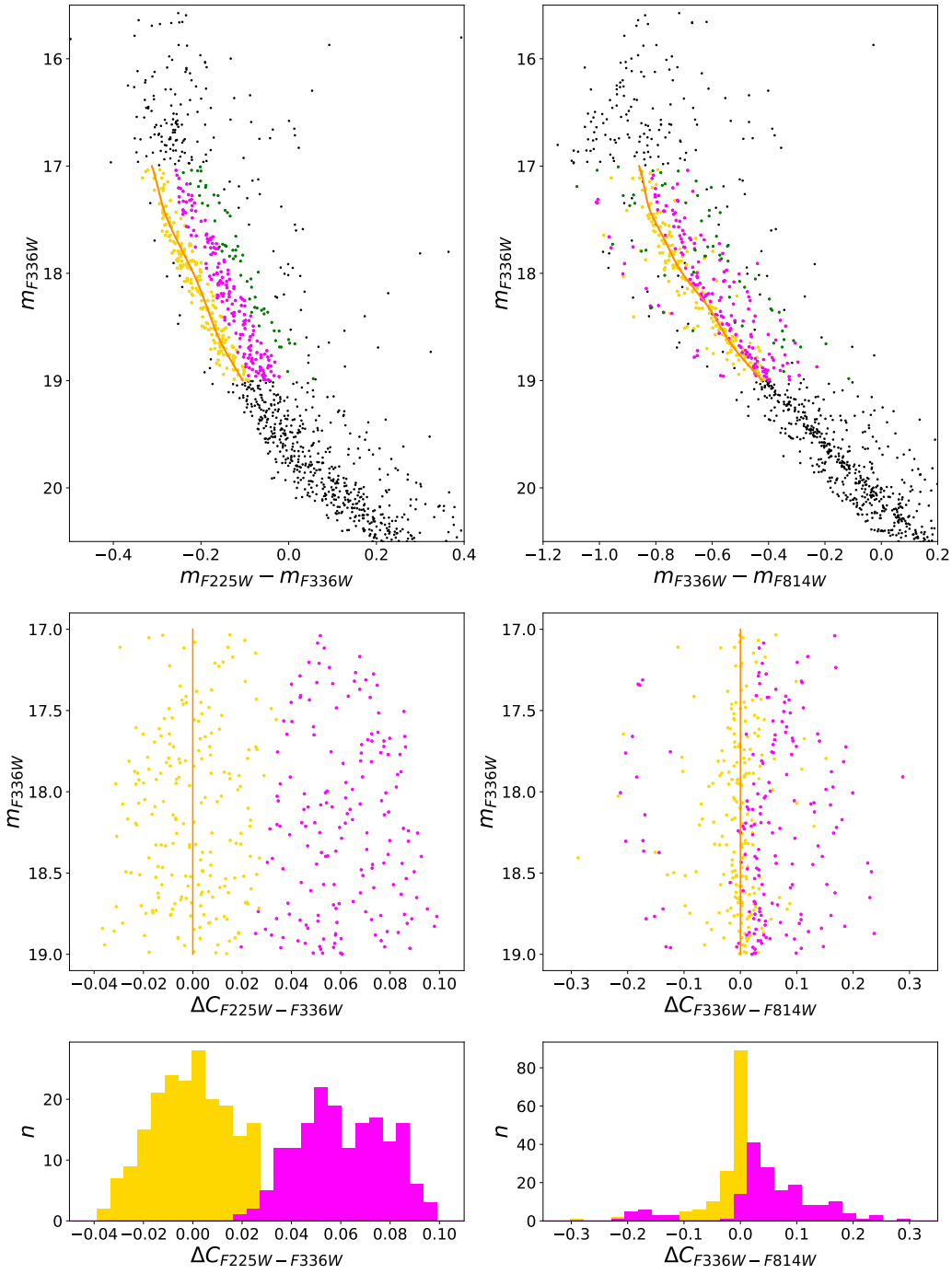

Figure 3.10: $m_{F225W} - m_{F336W}$ versus m_{F336W} CMD (upper-left panel) and $m_{F336W} - m_{F814W}$ versus m_{F336W} CMD (upper-right panel). The two sequences of bright MS stars selected from the upper-left CMD are colored yellow and magenta, while green points in the upper panels indicate candidate binary systems. Middle panels plot the verticalized $\Delta C_{F225W-F336W}$ versus m_{F336W} and $\Delta C_{F336W-F814W}$ versus m_{F336W} diagrams, and lower panels show the histogram distribution of the $\Delta C_{F336W-F814W}$ verticalized color. The verticalized diagrams are derived by using the fiducial lines of the yellow population (orange fiducial).

CHAPTER 4

Binaries among Multiple Populations in NGC 2164

The main purpose of this chapter is to derive the frequency of binaries among multiple populations, alias among the blue and red main sequences. This information will constrain one of the main scenarios for the origin of multiple sequences in the CMDs of young clusters. In particular, I will understand whether the blue and the red MSs share similar populations of binary systems or if binaries are mostly associated with the blue MS, as expected if this sequence is composed of slow rotators that have been braked by tidal interaction in binary systems.

4.1 Analysis concept

As discussed in previous section 1.3, the possible responsible for the braking of stellar rotation are tight binaries with short periods. On the contrary, wide binaries behave like single stars and, due to their lower binding energy, are more likely disrupted in the dense environment of the cluster. For these reasons, the binary systems analyzed in this work are unresolved stellar systems that appear as point-like sources. Their position in the CMD is related to the luminosity of their two components. In the case of non-interacting binary stars the magnitude of the system is:

$$m_{bin} = -2.5 \cdot log(F_1 + F_2) \tag{4.1}$$

where F_1 and F_2 are the fluxes of the two components.

A binary system composed by two stars with the same luminosity will display a magnitude $m_{bin} = -2.5 \cdot log(2) \simeq 0.75$ mag brighter than the single stars while keeping the color constant. In a simple stellar population, equal-mass binaries define a sequence that runs parallel to the main sequence fiducial line, but 0.75 mag brighter. Binaries composed of two stars with different luminosities and masses (M_1 and M_2) are located between the MS fiducial line and the equal-mass binaries fiducial line. The exact position in the CMDs depends on the mass of the primary star and the mass ratio $q = \frac{M_2}{M_1} \leq 1$, as shown in Figure 4.1 taken from (Milone et al. 2012).

Figure 4.2 illustrates the method to disentangle binaries composed of fast-rotating and non-rotating stars. This method, is similar to the procedure adopted by (Milone et al. 2020) to derive the frequency of binaries among multiple stellar populations

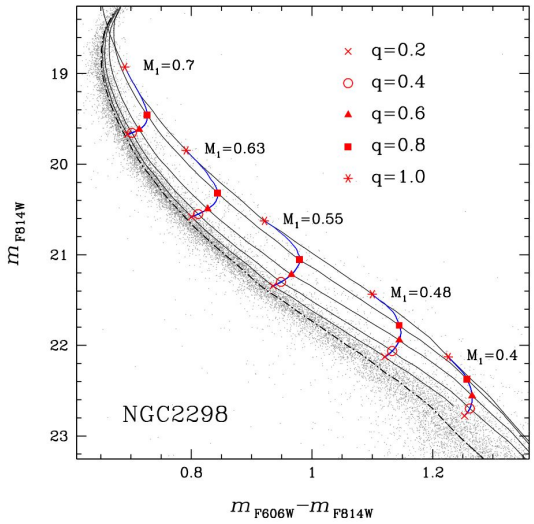

Figure 4.1: Binaries sequences as a function of the mass ratio $q = \frac{M_2}{M_1}$, with respect to the MS fiducial line indicated by the black dashed line. Taken from (Milone et al. 2012).

of old Galactic GCs. Panel (a) shows the fiducial line of the red MS (red continuous line) and the corresponding equal-mass binaries fiducial (red dotted line) in the $m_{F225W} - m_{F336W}$ versus m_{F336W} CMD. Two red-MS stars with magnitudes $m_{F336W} = 19.0$ and $m_{F336W} = 21.0$ are plotted with red-starred symbols, while the corresponding binary system is represented with the large starred symbol. Panel (b) provides the same information as panel (a), but for the $m_{F336W} - m_{F814W}$ versus m_{F814W} CMD. Lower panels (c) and (d) reproduce the upper ones, but I added the fiducial lines of single blue-MS stars and of equal-mass blue-MS binaries (blue continuous and dotted lines, respectively). An additional binary system, composed of two blue-MS stars, is represented with blue starred symbols.

Clearly, the two binary systems are indistinguishable from each other in the bottom-left CMD, where the color separation between the blue-MS and the red-MS binaries is comparable with the observational errors. On the contrary, the two binary systems are well separated in the bottom-right CMD. In the next section, I will take advantage from the behaviour of binaries in these two CMDs to estimate the frequency of binaries among red-MS and blue-MS stars.

4.2 Analysis

In this section, I apply the method above to the photometry of NGC 2164. I first select the sample of red-MS, blue-MS and binary stars from the observed CMD. Then, I compare the color distributions of the observed binaries and of a grid of simulated populations of binaries that comprise various fractions of bMS-bMS and rMS-rMS binaries.

4.2.1 CMD choice

From the various combinations of the available magnitudes I can build 24 CMDs, 9 with the wide-band filters, and the remaining ones including the narrow-band filter.

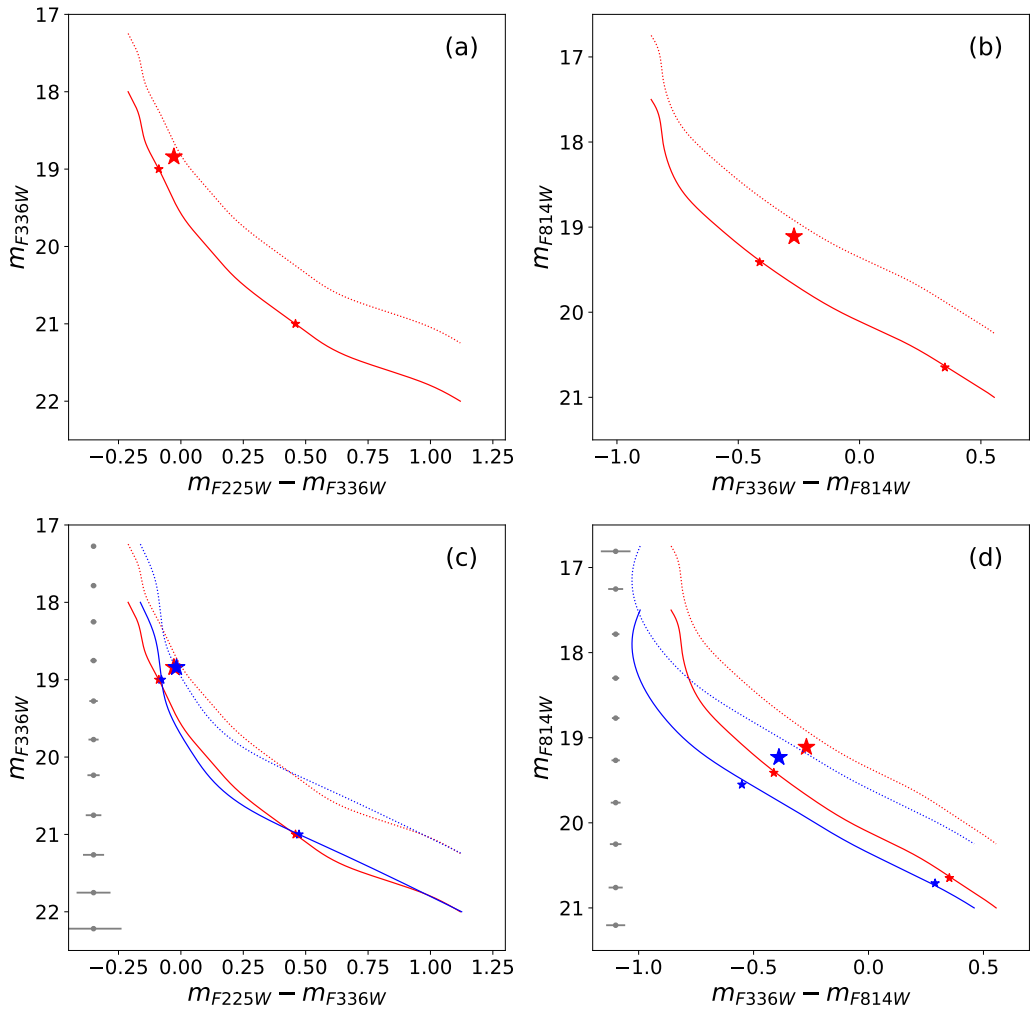

Figure 4.2: This figure illustrates the behaviour of binary systems composed of two red-MS stars (red starred symbols) and two blue-MS stars (blue starred symbols) in the $m_{\rm F336W}$ vs. $m_{\rm F225W} - m_{F336W}$ (left panels) and the $m_{\rm F814W}$ vs. $m_{\rm F336W} - m_{F814W}$ CMD (right panels). The two components of each binary system have magnitudes $m_{F336W} = 19.0$ and $m_{F336W} = 21.0$ and are represented with small starred symbols, whereas the resulting binaries are plotted with large starred symbols. The blue and red continuous lines are the fiducials of the blue- and red-MS, respectively, and the dotted lines of the same color represent the corresponding fiducials of equal-mass binaries. Upper panels show the binaries composed of two red-MS stars alone, while in the bottom panels, I also include binary systems made of pairs of blue-MS stars. Clearly, the two binaries exhibit similar $m_{\rm F225W} - m_{F336W}$ colors, but are well separated in the right-panel CMD.

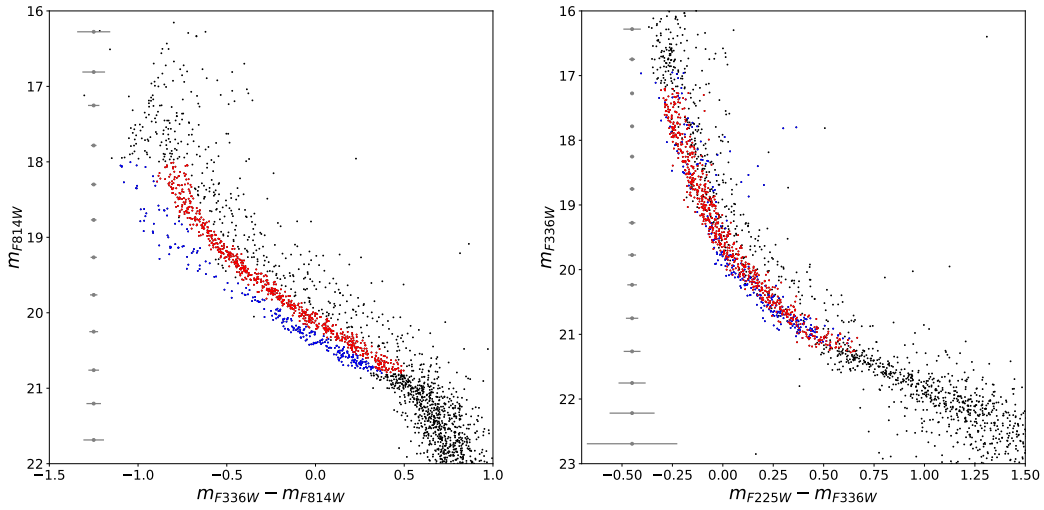

Figure 4.3: CMDs of NGC 2164 obtained with different combinations of filters: $m_{F336W} - m_{F814W}$ versus m_{F814W} in left-hand panel, $m_{F225W} - m_{F336W}$ versus m_{F336W} in right-hand panel. This figure shows that the choice of colours affects the separation of the two main sequences.

Among them, the most-suitable diagrams for my purpose are the $m_{F336W} - m_{F814W}$ versus m_{F814W} CMD, where the split MS is more evident, and the $m_{F225W} - m_{F336W}$ versus m_{F336W} CMD, where the two sequences are almost blended together. These are plotted in Figure 4.3.

The selection of red- and blue-MS stars has been performed from the left-panel CMD, tracing by eye the blue and red boundaries to each sequence. I only select stars in the m_{F814W} magnitude interval between the MS bend and the turn off, where the split is evident.

4.2.2 Binary region determination

Only binaries with relatively high mass ratio, which populate appropriate regions of the CMDs, may provide information on multiple populations. To select the appropriate CMD region, I exploit the $m_{F225W} - m_{F336W}$ versus m_{F336W} CMD, where the two MSs are nearly coincident. This region is represented with the yellow shaded area in the left panel of Figure 4.4, and its boundaries are derived as follows.

- The bright boundary is set at $m_{F336W} = 18.5$, as for brighter magnitudes binary stars are mixed with MS single stars and eMSTO stars.
- The faint boundary is set at $m_{F336W} = 19.75$. Based on artificial-star experiments I verified that, due to observational uncertainties, it is challenging to disentangle blue- and red-MS binaries with fainter magnitudes.
- The blue limit is determined by the MS fiducial line (black continuous line) shifted towards redder colors by seven times the color photometric error at each magnitude.
- The red boundary is determined by the equal mass binaries fiducial line (traced with a black dashed line) shifted towards redder colors by five times the color

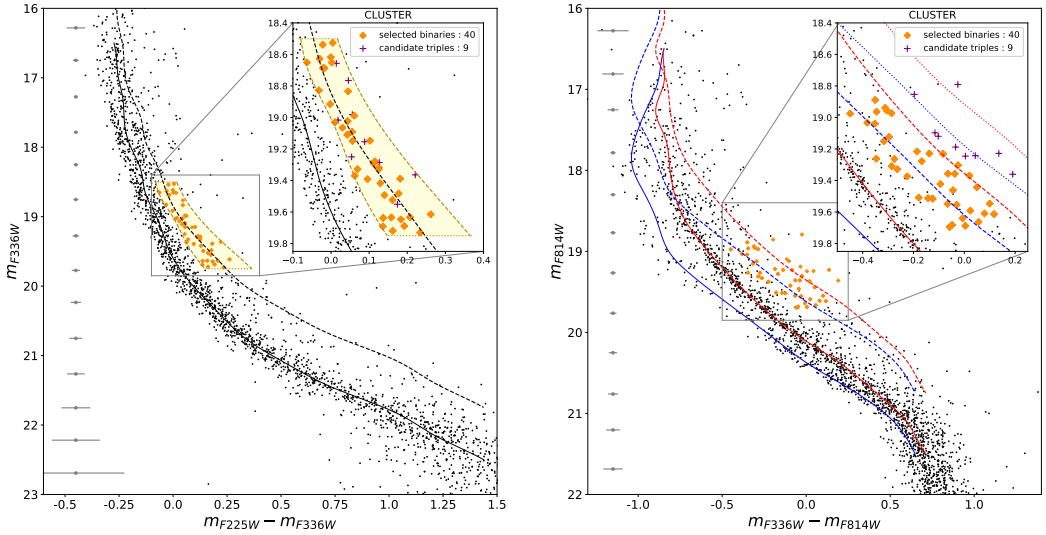

Figure 4.4: Selection of binary candidates in NGC 2164 from $m_{F225W} - m_{F336W}$ versus m_{F336W} CMD (left panel) and distribution of the selected stars along binaries sequences in $m_{F336W} - m_{F814W}$ versus m_{F814W} CMD (right panel). Black lines in the right-panel CMD indicate the fiducial of all MS stars and the corresponding fiducial of equal-mass binaries. Blue and red fiducials superimposed on the right-panel CMD are derived from blue-MS and red-MS stars, respectively. The fiducial lines for all stars in the left CMD and for blue MS Same colors dashed lines represent the corresponding fiducial lines for the equal-mass binaries sequences; with dotted lines, in right panel's inset, are also plotted the equal-mass triple systems fiducials.

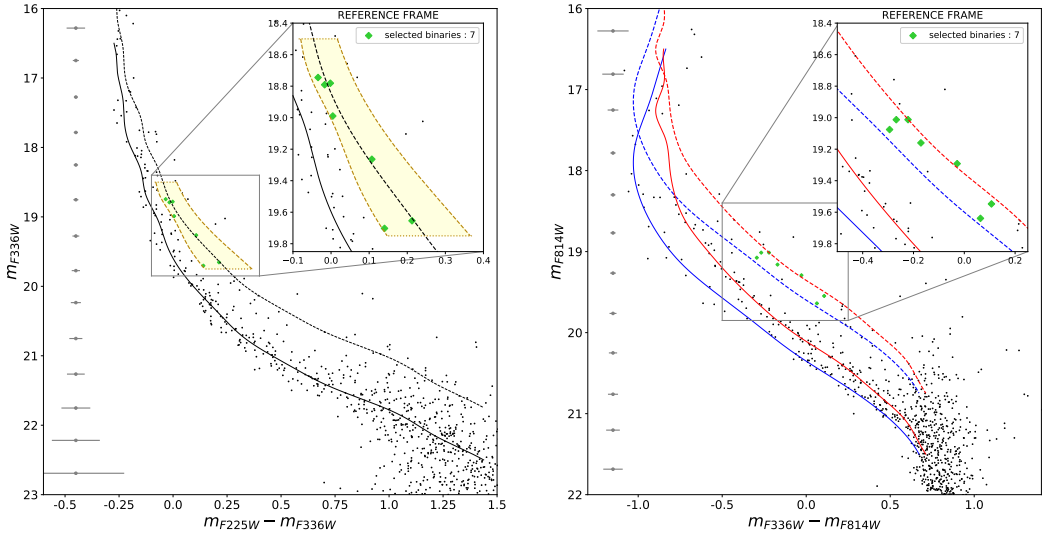

Figure 4.5: Fiducial lines and limits of the binaries selection region are the same as in figure 4.4, but plotted stars and selected binaries (green diamonds) are those in the field reference frame.

photometric error at each magnitude.

The choice of the left and right boundaries is based on the criteria of minimizing the contamination of the binary sample from single MS stars and from field stars.

The resulting sample comprises 52 candidate binary systems. Based on the $m_{F336W} - m_{F814W}$ versus m_{F814W} CMD, I verify that three selected stars lie on the blue MS. Hence, I exclude these outliers from the following analysis. Moreover, I note that these three stars fall inside the yellow shaded region close to its upper boundary, indicating that extending this selection to more luminous stars is of no use to increase the sample of binaries.

To further investigate the 49 candidate binaries, I derive the verticalized $m_{\rm F814W}$ vs. $\Delta C_{F336W-F814W}$ diagram, in such a way that the fiducial lines of equal-mass blue-MS binaries and red-MS binaries translate into a vertical line with abscissa equal to zero and one, respectively. Nine candidate binaries displays much redder colors than the red equal-mass binaries fiducial line. These are likely field stars or triple systems: I plot them with purple crosses in Figure 4.4 and exclude them from the successive analysis of binaries. For indication, I plot with dotted lines, in the right panel's inset, also the fiducial lines for equal-mass triple systems, both for the blue and red MSs. The final sample consists in 40 binary system candidates in the cluster region.

In Figure 4.5 are the selected field stars in the reference field that populate the yellow shaded region. To do this, I use the same procedure and the same boundaries derived for stars in the cluster field. I identified eight stars in the yellow region of the reference-field CMD, including a blue MS star. This outlier has been removed from the list, in close analogy with what I did for the cluster field analysis. The remaining seven stars are used to account for contamination from field stars in the sample of candidate NGC 2164 binaries.

4.2.3 The color distribution of binary stars

Left panel of figure 4.6 shows all selected stars, including candidate binaries of the cluster and field stars in the reference field in the $m_{F336W} - m_{F814W}$ versus m_{F814W} CMD. This CMD maximizes the color separation between the rMS and the bMS, and between the corresponding binaries fiducials. Top right panel shows their positions in the verticalized m_{F814W} vs $\Delta C_{F336W-F814W}$ diagram. The quantity $\Delta C_{F336W-F814W}$ is calculated as the normalized distance from the blue and red equal-mass binaries fiducial lines, at each magnitude, where these are set at $\Delta C_{F336W-F814W} = 0$ and 1 respectively. The abscissa of each binary is then:

$$\Delta C^{bin}_{F336W-F814W} = \frac{C \;-\; C^{bMS-bMS}_{fiducial}}{C^{bMS-bMS}_{fiducial} - C^{rMS-rMS}_{fiducial}} \tag{4.2}$$

where C indicates the color $m_{F336W} - m_{F814W}$ measured in the left-hand panel CMD.
Lower right panels show the kernel-density, ϕ, and the cumulative distributions, ρ, of the $\Delta C_{F336W-F814W}$ pseudo-color. The kernel-density is derived by a Gaussian kernel function with a width factor of 2.

Orange lines represent the distributions of the candidate binaries in the cluster field, whereas green lines mark the distributions of the selected stars in the reference

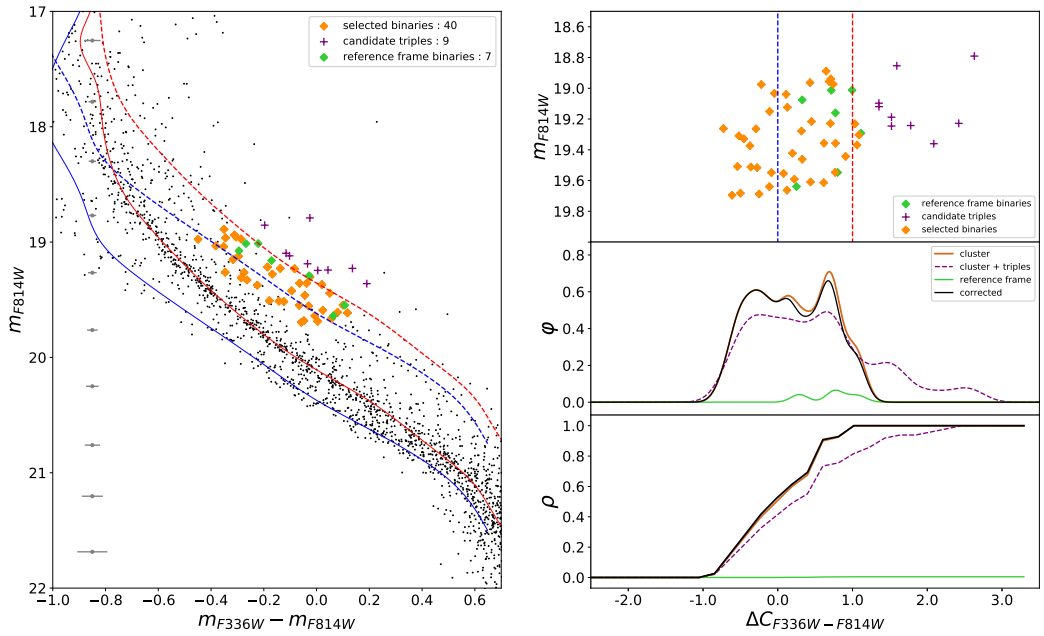

Figure 4.6: Left panel: $m_{F336W} - m_{F814W}$ versus m_{F814W} CMD of NGC 2164. Blue and red continuous lines are the fiducials of the red- and blue-MS, respectively, while dashed lines are the respective equal-mass binaries fiducials. All stars in the binary region are indicated with colored symbols. Orange diamonds are candidate binaries in the cluster region, green diamonds are the selected stars in the reference field and purple crosses mark candidate triple systems. Right panels show in order: the verticalized distribution on the pseudo-color $\Delta C_{F336W-F814W}$ (top), the kernel-density (middle) and the cumulative distribution (bottom).

field. To account both for the different areas of the cluster and the reference field I normalize the ratio between the areas (as defined in Figure 3.2, $A^{field}_{>54"}/A^{cluster}_{<36"} = 4.19$). The black line is the cluster distribution corrected from field contamination by subtracting the orange and green distributions.
For illustration purposes only, I show the distribution of the cluster sample including the candidate triple-systems with (purple dashed line).

Clearly, the distribution of $\Delta C_{F336W-F814W}$ is not consistent with a single population. Indeed, neither bMS-bMS binaries (for which the distribution would be a single picked Gaussian centered on $\Delta C_{F336W-F814W} = 0$) nor rMS-rMS binaries (centered on $\Delta C_{F336W-F814W} = 1$) alone can reproduce the derived distribution. Actually, the wider kernel-density gives hint for a bimodal distribution.

4.3 Measuring the frequency of binaries among the distinct populations

To infer the fraction of bMS-bMS and rMS-rMS binaries with respect to their total number, I compare the $\Delta C_{F336W-F814W}$ distribution of the observed binaries, with a grid of simulated diagrams derived from artificial stars.

4.3.1 Artificial Star tests

Artificial-star (AS) experiments are performed to generate synthetic CMDs and are derived from a catalog containing positions and fluxes of 45,000 ASs. I assumed for ASs the same F814W luminosity distribution as derived for the real stars and calculated the corresponding colors from the fiducial lines of red-MS and blue-MS stars. Moreover, I adopted the same radial distribution for the ASs as observed for the real stars in close analogy to (Milone et al. 2009)

Photometry and astrometry of ASs have been carried out as in (Anderson et al. 2008) by adopting the same computer programs and the same methods by Anderson and collaborators that have been used for real stars and described in Chapter 2. I considered an AS as recovered if the measured flux and position differ by less than 0.75 mag and 0.5 pixel, respectively, from the corresponding input values.

Binaries are then obtained by coupling pair of stars belonging to the same population and by assuming a flat mass ratio distribution as derived for old Globular clusters (Milone et al. 2012, 2016).

Only simulated binary stars and single stars within the cluster region (i.e. within two half-light radii from the cluster center), that lie within the yellow dashed area of the CMD are included in the analysis. The numbers of stars that pass these criteria of selection are provided in Table 4.1.

4.3.2 Simulations

I generate a grid of CMDs with different fractions of bMS-bMS ($f^{bMS-bMS}_{bin}$) and rMS-rMS stars ($f^{rMS-rMS}_{bin}$) . In particular, I assumed that $f^{rMS-rMS}_{bin}$ ranges from 0 to 1 in steps of 0.01 and $f^{bMS-bMS}_{bin} = 1 - f^{rMS-rMS}_{bin}$. For each of diagram, I calculate the $\Delta C_{F336W-F814W}$ quantity and the corresponding kernel-density and cumulative distributions, in close analogy with what I did for real stars.

The simulated distributions are compared with the observed one by means of a

Object	Total	$\in$ binary region	$r < 2\,r_{hl}$
N_{star}^{bMS}	45000	40	29
N_{star}^{rMS}	45000	25	19
$N_{bin}^{bMS-bMS}$	45000	1970	1367
$N_{bin}^{rMS-rMS}$	45000	4481	3275

Table 4.1: Artificial single stars and binaries catalogs.

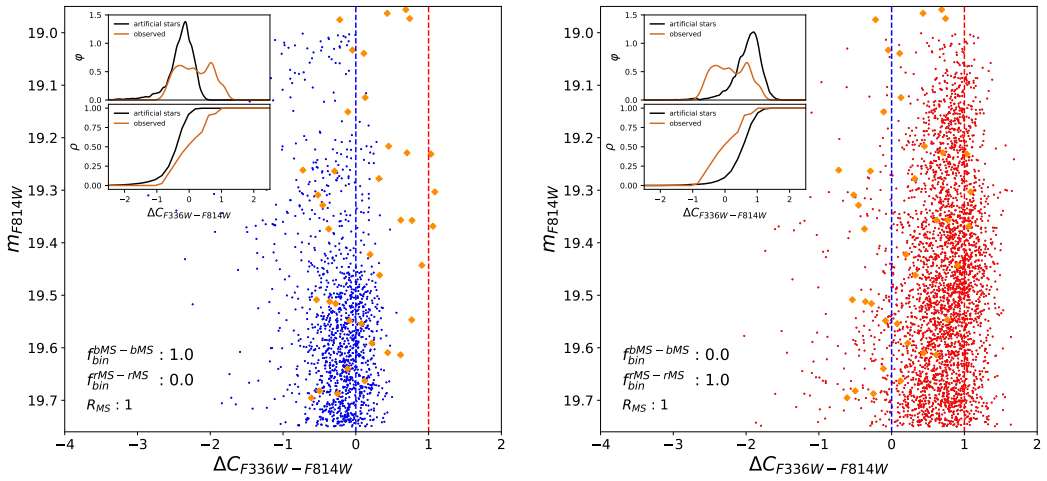

Figure 4.7: m_{F814W} vs. $\Delta C_{F336W-F814W}$ for simulated bMS-bMS (blue points) and rMS-rMS binaries (red points) and for observed binaries (orange dots). Left and right panels show two extreme simulations composed of bMS-bMS and rMS-rMS binaries alone. The kernel density and cumulative distributions of simulated (black lines) and observed binaries (orange lines) are compared in the insets. In the simulations I assumed the same fraction of rMS and bMS stars ($R_{MS} = 1$)

least χ^2:

$$\chi^2_{\phi} = \frac{\Sigma(\phi_{obs} - \phi_{AS})^2}{n_{bins}} \tag{4.3}$$

and

$$\chi^2_{\rho} = \frac{\Sigma(\rho_{obs} - \rho_{AS})^2}{n_{bins}} \tag{4.4}$$

for kernel-density and cumulative distributions respectively. Here, $n_{bins} = 30$, is the number of $\Delta C_{F336W-F814W}$ intervals used to derive each distribution.

As an example, in Figure 4.7 I show the simulated m_{F814W} versus $\Delta C_{F336W-F814W}$ pseudo-color diagrams for two extreme distributions of binaries; the diagram on the left hosts *rMS-rMS* binaries alone, whereas the right-panel CMD is entirely composed of *bMS-bMS* binaries. I also show the observed binaries (orange diamonds) and provide the kernel-density and cumulative distributions for the observed and simulated binaries (orange and black lines, respectively).

To identify the simulation that provides the best match with the observed CMD, I plot in Figure 4.8 the χ^2 values against the fraction of bMS binaries. Both χ^2 deter-

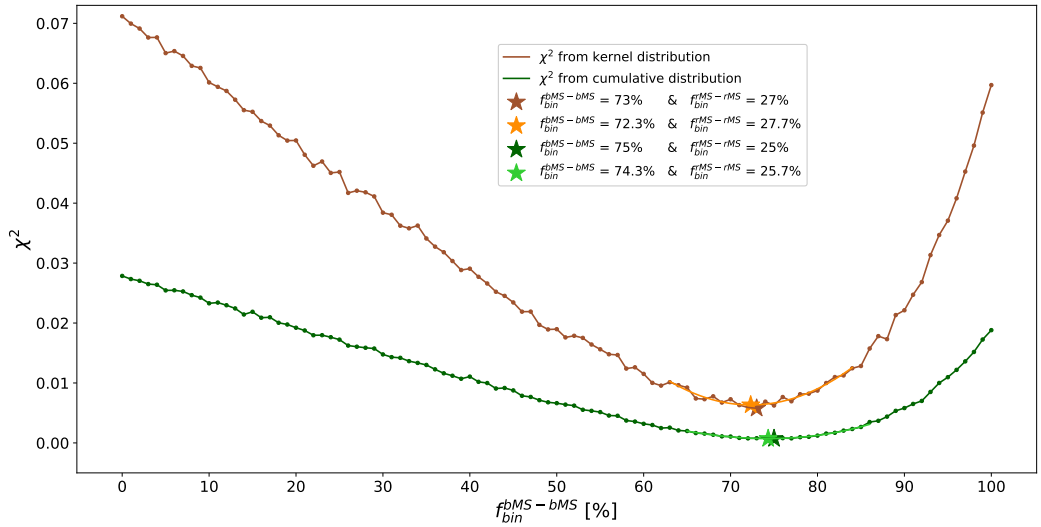

Figure 4.8: This figure illustrate the procedure to identify the simulation that best reproduces the observed distribution of binary stars. Here the χ^2 values from the kernel-density distribution (brown) and the cumulative distribution (brown) are plotted against the fraction of bMS binaries. Their minimum values are indicated by the starred symbol with the same color. Ochre and light-green lines are cubic interpolations of the ten points closest to the minimum χ^2. The minimum χ^2 values derived from the interpolation are marked by ochre and light-green starred symbols.

minations from the kernel distribution (brown line) and the cumulative distribution (green line) exhibit low values for $f_{bin}^{bMS-bMS} \sim 0.65 - 0.85$. I used a cubic function to fit a portion of the curve that includes the twenty points closest to the minimum. The minimum χ^2 value inferred from the kernel-density distribution and the cumulative distribution in provided by a fraction of bMS binaries of 0.72 and 0.74, respectively. Figure 4.9 compares the observed binaries with the simulated diagram with $f_{bin}^{bMS-bMS} = 0.73$ in the m_{F814W} vs. $\Delta C_{F336W-F814W}$ plane.

To derive the frequency of bMS binaries, $\widehat{f}_{bin}^{bMS-bMS}$, I account for the observed ratio of bMS over rMS stars, $R_{MS} = 4$, by using two different approaches. The first consists in using the fractions of bMS and rMS above and the relation:

$$\widehat{f}_{bin}^{bMS-bMS} = (1 + \frac{f_{bin}^{rMS-rMS}}{f_{bin}^{bMS-bMS} \cdot R_{MS}})^{-1} \tag{4.5}$$

To maximize the statistical significance of the result, I repeated the analysis 25 times and consider the average value inferred from these binary-fraction determinations. The results from each simulation are summarized in Table 4.2.

I obtain a percentage of $\widehat{f}_{bin}^{bMS-bMS} = 91.4\%$ and $\widehat{f}_{bin}^{rMS-rMS} = 8.6\%$ from the kernel-density distribution, and of $\widehat{f}_{bin}^{bMS-bMS} = 92.1\%$ and $\widehat{f}_{bin}^{rMS-rMS} = 7.9\%$ from the cumulative distribution.

As an alternative method to account for the observed fractions of bMS and rMS stars, I repeat the procedure above but using a fraction of rMS stars that is four times more populous than the the bMS, as in the observed CMD. The minimum χ

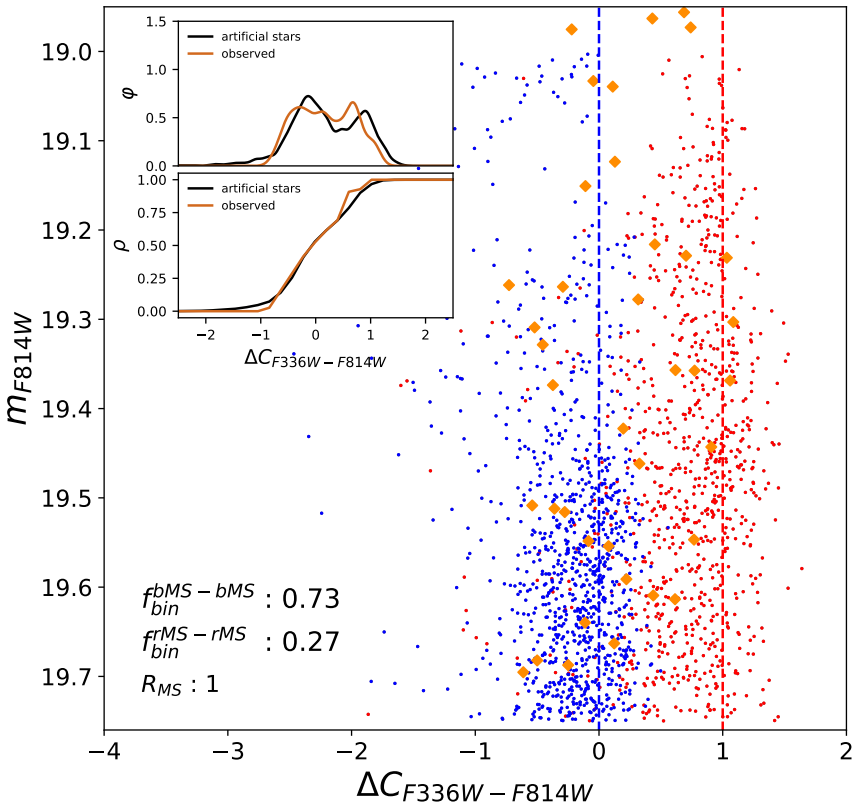

Figure 4.9: As in Figure 4.7, but for the best-fit simulation.

square corresponds to $f_{bin}^{bMS-bMS} = 91.2\%$ and $f_{bin}^{rMS-rMS} = 8.8\%$ from the kernel-density distribution, and of $f_{bin}^{bMS-bMS} = 91.9\%$ and $f_{bin}^{rMS-rMS} = 8.1\%$ from the cumulative distribution (Figure 4.11), in excellent agreement with results from the previous method.

The resulting best-fit m_{F814W} vs. $\Delta C_{F336W-F814W}$ diagrams is plotted in Figure 4.12. For completeness I plot in Figure4.11 the simulations relative to the extreme cases, where all binaries belong to red MS and to the blue MS.

4.3.3 Uncertainties

To derive the uncertainties associated to the bMS and rMS binary frequency, I apply two methods based on bootstrap and Montecarlo simulations. Results from each method are listed in Table 4.3 alongside with the results from the artificial stars simulations.

Bootstrap simulation The *Bootstrap* analysis is based on the following procedure: first, I use the 40 observed binaries to generate a catalog of 40,000 binaries composed of 1,000 replica of the original sample.
Then, I randomly extract 40 binaries from this catalog and estimate the frequency of bMS and rMS by using the same procedure adopted for real stars. I repeat this procedure 1,000 times. I assume that the uncertainty to the measured values of $f_{bin}^{bMS-bMS}$ and $f_{bin}^{rMS-rMS}$ is provided by the standard deviation of the 1,000 deter-

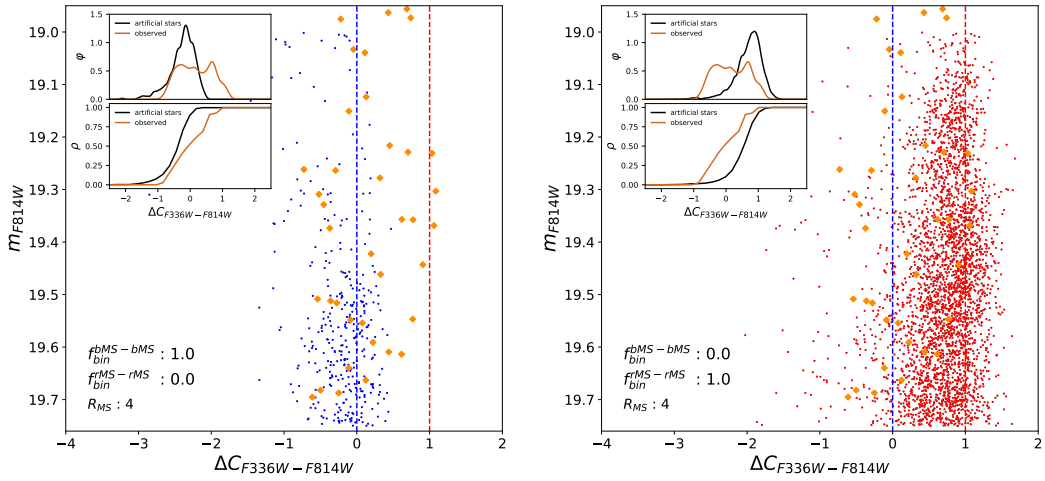

Figure 4.10: As in Figure 4.7 but by assuming the observed fractions of red-MS and blue-MS stars ($R_{MS} = 4$).

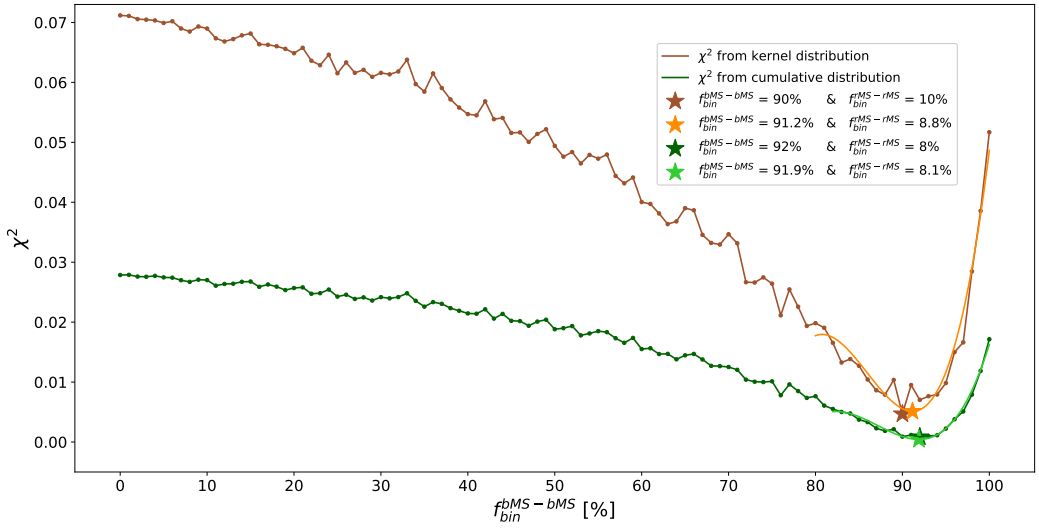

Figure 4.11: As for figure 4.8 but by assuming the observed fractions of red-MS and blue-MS stars ($R_{MS} = 4$).

Simulation	$R_{MS} = 1$				$R_{MS} = 4$			
#	kernel-density		cumulative		kernel-density		cumulative	
	least χ^2	interp.	least χ^2	interp.	least χ^2	interp.	least χ^2	interp.
1	71	71.7	75	74.2	90	91.4	93	92.0
2	73	73.3	73	74.4	91	91.8	93	92.1
3	72	72.9	74	74.5	91	91.5	91	91.9
4	71	72.3	74	74.6	91	91.1	92	92.0
5	74	73.2	75	74.9	92	91.3	92	91.8
6	73	72.7	73	74.7	93	92.0	92	92.0
7	73	72.8	73	74.5	93	92.0	93	92.2
8	69	72.1	74	74.5	92	91.6	92	91.9
9	71	72.7	75	74.8	91	91.6	91	91.7
10	75	73.1	75	74.7	90	91.1	93	92.4
11	77	73.4	73	74.8	93	92.0	93	91.9
12	76	72.8	73	74.5	90	91.4	90	91.5
13	76	73.0	73	74.7	93	91.9	93	92.3
14	71	73.2	75	74.9	92	91.7	92	92.0
15	73	72.2	74	74.6	93	91.7	92	91.9
16	77	72.7	73	74.2	93	92.1	92	92.2
17	72	72.8	76	74.7	91	91.4	92	91.6
18	73	71.6	76	74.6	92	91.4	91	91.8
19	70	72.2	77	74.7	94	92.0	92	92.0
20	74	72.2	74	74.4	91	91.6	92	92.1
21	71	72.0	75	74.7	92	91.7	92	92.1
22	75	73.0	75	74.5	91	91.3	91	91.9
23	71	72.8	74	75.0	89	91.0	93	92.2
24	72	71.9	75	74.5	92	91.7	93	92.2
25	70	72.1	73	74.2	92	91.3	92	92.0
mean	72.8	72.6	74.3	74.6	91.6	91.6	92.1	92.0
std	2.2	0.5	1.1	0.2	1.2	0.3	0.8	0.2

Table 4.2: results from 25 AS simulations. Note that last line reports the standard deviations of the above values, but these are not the uncertainties considered, which are instead computed by a bootstrap and montecarlo analysis, explained in section 4.3.3.

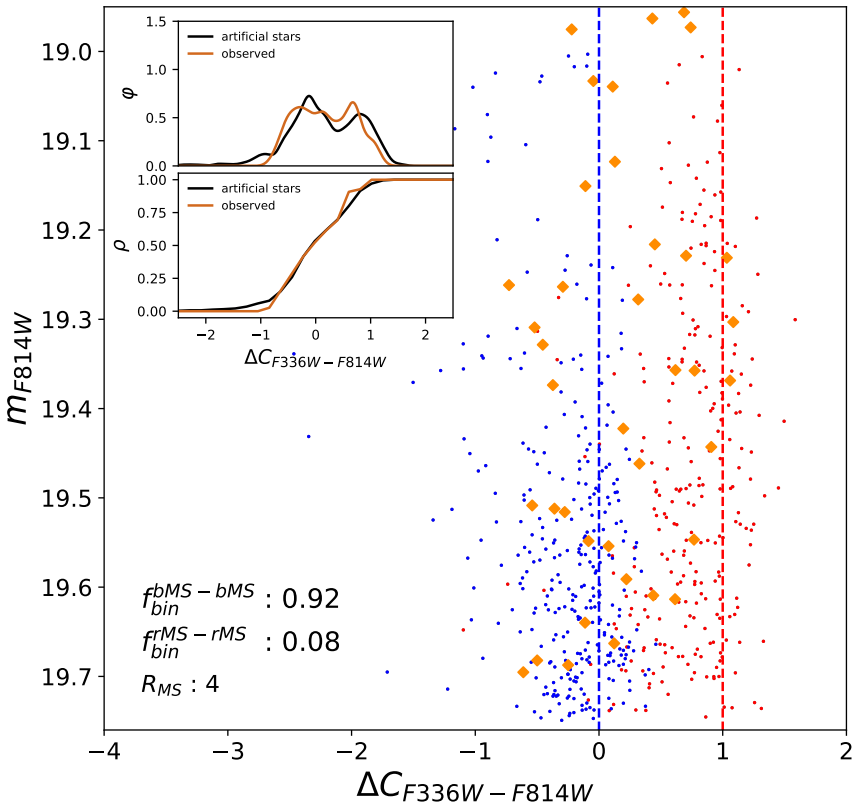

Figure 4.12: As for figure 4.9 but for the best-fit simulation obtained by assuming the observed fractions of red-MS and blue-MS stars ($R_{MS} = 4$).

minations of binaries frequency from the simulations. The uncertainty corresponds to ±3.5% for the results from the kernel-density distributions, and to ±2.8% for the results from the cumulative distribution.

Montecarlo simulation The *Montecarlo* analysis follows a different procedure: I start from the best distribution found from the precedent artificial stars simulation, that is $f_{bin}^{bMS-bMS} = 92\%$ and $f_{bin}^{rMS-rMS} = 8\%$ (with rounded values, as I consider steps of 1% in the grid of different compositions to run the simulation). I create an artificial binaries list reflecting this composition: that is a catalog with 92% of the total number of *bMS-bMS* binaries and with 8% of the total number of *rMS-rMS* binaries. Form this sample, that is composed of 576 artificial binaries, I then randomly pick 40 stars for which I recalculate the kernel-density and cumulative distributions, which will be the reference for a new artificial star simulation. I find the minimum χ^2 value and the corresponding best distribution. I run this entire procedure 1000 times, creating a new catalog from which picking the 40 reference stars every time. Finally I calculate the mean value and the standard deviation of the binaries fractions obtained through this procedure, and as for the *bootstrap* method these are the uncertainties associated to the previously found results. From this analysis I obtain the same value of the standard deviation of ±2.7% for both the results derived from the kernel-density those derived from the cumulative distribution.

distribution	population	percentage	uncertainties	
			Bootstrap	Montecarlo
kernel-density	$f_{bin}^{bMS-bMS}$	91.6	± 3.5	± 2.7
	$f_{bin}^{rMS-rMS}$	8.4	± 3.5	± 2.7
cumulative	$f_{bin}^{bMS-bMS}$	91.9	± 2.8	± 2.7
	$f_{bin}^{rMS-rMS}$	8.1	± 2.8	± 2.7

Table 4.3: Results

As stated before, the bootstrap analysis should give an overestimate of the uncertainties, while the montecarlo analysis an underestimate: indeed, uncertainties from the former method are larger, but similar to the latter. Moreover there is not a large difference (if not at all for the montecarlo-derived uncertainties) between the results derived from the kernel-density and cumulative distributions.

CHAPTER 5

Results and Discussion

5.1 Multiple populations in young clusters

The discovery that young and intermediate-age LMC and SMC clusters exhibit eMSTO has dramatically changed the long-held picture that star clusters are prototypes of simple stellar populations. The most straightforward interpretation is that the eMSTO is due to age spread. Hence, these clusters would host multiple generations of stars with different ages (e.g. Goudfrooij et al. 2011; Mackey et al. 2008; Milone et al. 2009). The most intriguing alternative is that all stars have the same ages but different rotation rates. Indeed, a range of stellar rotation can mimic an age spread in a population of coeval stars (e.g. Bastian et al. 2009).

The physical reason is that the limb darkening, a phenomenon due to the optical thickness of the atmosphere towards the center and the outskirts of a star, may produce a spread in color and magnitude for turn-off stars. In addition, gravity darkening causes the star to appear cooler and dimmer when viewed equator-on as compared to pole-on. As a consequence of both effects, a star seen pole–on will look bluer and brighter (hence hotter and brighter) than it would be if seen equator–on. By assuming that the rotation axis have random orientations, the combined effect of limb darkening and gravity darkening would reproduce the observed eMSTOs (e.g. D'Antona et al. 2015; Georgy et al. 2019).

The discovery of a double main sequences in clusters younger than about 800 Myr added an important piece to this puzzle (e.g. Milone et al. 2015a, 2018). Indeed, the split MSs are the signature of stellar populations with different rotation rates, as confirmed by direct spectroscopic determinations of stellar rotation (e.g Dupree et al. 2017; Marino et al. 2018a,b).

A strongly debated question is whether the eMSTO is entirely due to rotation or if age spread, in addition to rotation, is needed to match the observations. Indeed, stellar models that include rotations alone do not entirely reproduce the eMSTOs.

A possible solution, is provided by D'Antona et al. 2017 who have interpreted the non-rotating MS as stars initially rapidly rotating, that have later slowed down. This scenario would explain the eMSTO phenomenon without invoking an age difference.

In this scenario, interactions in binary stars could be the responsible for stellar braking. Hence, we would expect a predominance of binaries among the blue MS.

5.2 Binaries among multiple populations in NGC 2164

In this thesis, I constrain the "braking" scenario by deriving, for the first time, the frequency of binaries among the blue and red MS of a young LMC cluster with an eMSTO.

I analyzed high-precision photometry of NGC 2164, derived from images collected through three wide-band filters and one narrow-band filter of the UVIS channel of WFC3 on board *HST*. I adapted to NGC 2164, the method introduced by Milone et al. 2020 to study binaries among multiple populations in old Galactic GCs. Specifically, I exploited the $m_{F225W} - m_{F336W}$ vs. m_{F336W} CMD, where the two MSs of NGC 2164 are nearly coincident, to select an appropriate sample of binaries. Then, I used the $m_{F336W} - m_{F814W}$ vs. m_{F814W} CMD, which maximizes the color separation between the two MSs, to disentangle binaries among the distinct populations.

The comparison of the color distribution of observed binaries and a grid of simulated CMDs with different compositions has allowed me to derive, for the first time, the frequency of binaries among the red- and the blue-MS of NGC 2164

I find that $\sim 73\%$ of the analyzed binaries belong to the bMS. Since the bMS hosts about one forth of the total number of MS stars in the analyzed magnitude interval, I conclude that the relative frequency of *bMS-bMS* binaries is $92 \pm 3\%$.

I verify that this conclusion does not depend on the method used to compare the observations and the simulated CMDs. Final results of this analysis are summarized in Table 4.3.

The results presented in this thesis provide strong evidence for the prevalence of binary systems among the slowly or non-rotating stellar population composing the blue MS. This finding supports the "braking" scenario, where tidal interaction in binary systems is the most efficient mechanism in braking stellar rotation. In this context, I suggests that the blue MS is mostly or entirely composed of binaries with small mass ratios.

As a by side result of my investigation of this high precision photometric dataset, I report the discovery of a new feature in the CMD of NGC 2164. Indeed, the upper part of the red MS is broadened in the $m_{F225W} - m_{F336W}$ color with some hints of MS splits. This finding shows that the bright MS of NGC 2164 hosts at least three main components, in contrast with previous evidence of a split MS. Future investigation is needed to understand the physical reason of the triple MS.

Bibliography

Abt, Helmut A. et al. (Nov. 2004). "Tidal Effects in Binaries of Various Periods". In: *apj* 616.1, pp. 562–566. DOI: 10.1086/423795.

Anderson, Jay et al. (Oct. 2000). "Toward High-Precision Astrometry with WFPC2. I. Deriving an Accurate Point-Spread Function". In: 112.776, pp. 1360–1382. DOI: 10.1086/316632. arXiv: astro-ph/0006325 [astro-ph].

— (Feb. 2006). *PSFs, Photometry, and Astronomy for the ACS/WFC*. Instrument Science Report ACS 2006-01.

Anderson, Jay et al. (June 2008). "The Acs Survey of Globular Clusters. V. Generating a Comprehensive Star Catalog for each Cluster". In: *aj* 135.6, pp. 2055–2073. DOI: 10.1088/0004-6256/135/6/2055. arXiv: 0804.2025 [astro-ph].

Anderson, Jay et al. (Sept. 2010). *An Empirical Pixel-Based Correction for Imperfect CTE. I. HST's Advanced Camera for Surveys*. Instrument Science Report ACS 2010-03.

Bastian, N. et al. (Sept. 2009). "The effect of stellar rotation on colour-magnitude diagrams: on the apparent presence of multiple populations in intermediate age stellar clusters". In: *mnras* 398.1, pp. L11–L15. DOI: 10.1111/j.1745-3933.2009.00696.x. arXiv: 0906.1590 [astro-ph.GA].

Brandt, Timothy D. et al. (July 2015). "Rotating Stellar Models Can Account for the Extended Main-sequence Turnoffs in Intermediate-age Clusters". In: *apj* 807.1, 25, p. 25. DOI: 10.1088/0004-637X/807/1/25. arXiv: 1504.04375 [astro-ph.SR].

D'Antona, F. et al. (Jan. 2002). "The Böhm-Vitense Gap: The Role of Turbulent Convection". In: *apjl* 564.2, pp. L93–L96. DOI: 10.1086/338911.

D'Antona, F. et al. (Nov. 2015). "The extended main-sequence turn-off cluster NGC 1856: rotational evolution in a coeval stellar ensemble". In: *mnras* 453.3, pp. 2637–2643. DOI: 10.1093/mnras/stv1794. arXiv: 1508.01932 [astro-ph.SR].

D'Antona, F. et al. (Aug. 2017). "Stars caught in the braking stage in young Magellanic Cloud clusters". In: *Nature Astronomy* 1, 0186, p. 0186. DOI: 10.1038/s41550-017-0186. arXiv: 1707.07711 [astro-ph.SR].

D'Antona, F. et al. (Jan. 2018). "Braking stars in the Young Magellanic Cloud Massive Clusters". In: *memsai* 89, p. 42.

Dupree, A. K. et al. (Sept. 2017). "NGC 1866: First Spectroscopic Detection of Fast-rotating Stars in a Young LMC Cluster". In: *apjl* 846.1, L1, p. L1. DOI: 10.3847/2041-8213/aa85dd. arXiv: 1708.03386 [astro-ph.GA].

Ekström, S. et al. (Jan. 2012). "Grids of stellar models with rotation. I. Models from 0.8 to 120 M at solar metallicity (Z = 0.014)". In: *aap* 537, A146, A146. DOI: 10.1051/0004-6361/201117751. arXiv: 1110.5049 [astro-ph.SR].

Georgy, C. et al. (Feb. 2019). "Disappearance of the extended main sequence turn-off in intermediate age clusters as a consequence of magnetic braking". In: *aap* 622, A66, A66. DOI: 10.1051/0004-6361/201834505. arXiv: 1812.05544 [astro-ph.SR].

Girardi, Léo et al. (Mar. 2009). "Discovery of two distinct red clumps in NGC 419: a rare snapshot of a cluster at the onset of degeneracy". In: *mnras* 394.1, pp. L74–L78. DOI: 10.1111/j.1745-3933.2008.00614.x. arXiv: 0901.0773 [astro-ph.SR].

Girardi, Léo et al. (Mar. 2011). "Can rotation explain the multiple main-sequence turn-offs of Magellanic Cloud star clusters?" In: *mnras* 412.1, pp. L103–L107. DOI: 10.1111/j.1745-3933.2011.01013.x. arXiv: 1101.1880 [astro-ph.SR].

Goudfrooij, Paul et al. (Aug. 2011). "Population Parameters of Intermediate-age Star Clusters in the Large Magellanic Cloud. III. Dynamical Evidence for a Range of Ages Being Responsible for Extended Main-sequence Turnoffs". In: *apj* 737.1, 4, p. 4. DOI: 10.1088/0004-637X/737/1/4. arXiv: 1105.1317 [astro-ph.SR].

Goudfrooij, Paul et al. (Dec. 2014). "Extended Main Sequence Turnoffs in Intermediate-age Star Clusters: A Correlation between Turnoff Width and Early Escape Velocity". In: *apj* 797.1, 35, p. 35. DOI: 10.1088/0004-637X/797/1/35. arXiv: 1410.3840 [astro-ph.SR].

Mackey, A. D. et al. (July 2007). "A double main-sequence turn-off in the rich star cluster NGC 1846 in the Large Magellanic Cloud". In: *mnras* 379.1, pp. 151–158. DOI: 10.1111/j.1365-2966.2007.11915.x. arXiv: 0704.3360 [astro-ph].

Mackey, A. D. et al. (July 2008). "Multiple Stellar Populations in Three Rich Large Magellanic Cloud Star Clusters". In: *apjl* 681.1, p. L17. DOI: 10.1086/590343. arXiv: 0804.3475 [astro-ph].

Marino, A. F. et al. (Nov. 2008). "Spectroscopic and photometric evidence of two stellar populations in the Galactic globular cluster NGC 6121 (M 4)". In: *aap* 490.2, pp. 625–640. DOI: 10.1051/0004-6361:200810389. arXiv: 0808.1414 [astro-ph].

Marino, A. F. et al. (Sept. 2018a). "Different Stellar Rotations in the Two Main Sequences of the Young Globular Cluster NGC 1818: The First Direct Spectroscopic Evidence". In: *aj* 156.3, 116, p. 116. DOI: 10.3847/1538-3881/aad3cd. arXiv: 1807.04493 [astro-ph.SR].

Marino, A. F. et al. (Aug. 2018b). "Discovery of Extended Main Sequence Turnoffs in Galactic Open Clusters". In: *apjl* 863.2, L33, p. L33. DOI: 10.3847/2041-8213/aad868. arXiv: 1807.05888 [astro-ph.SR].

Martocchia, S. et al. (July 2018). "The search for multiple populations in Magellanic Cloud clusters - IV. Coeval multiple stellar populations in the young star cluster NGC 1978". In: *mnras* 477.4, pp. 4696–4705. DOI: 10.1093/mnras/sty916. arXiv: 1804.04141 [astro-ph.SR].

McLaughlin, Dean E. et al. (Dec. 2005). "Resolved Massive Star Clusters in the Milky Way and Its Satellites: Brightness Profiles and a Catalog of Fundamental Parameters". In: *apjs* 161.2, pp. 304–360. DOI: 10.1086/497429. arXiv: astro-ph/0605132 [astro-ph].

Milone, A. P. et al. (Apr. 2009). "Multiple stellar populations in Magellanic Cloud clusters. I. An ordinary feature for intermediate age globulars in the LMC?" In: *aap* 497.3, pp. 755–771. DOI: 10.1051/0004-6361/200810870. arXiv: 0810.2558 [astro-ph].

Milone, A. P. et al. (Apr. 2012). "The ACS survey of Galactic globular clusters. XII. Photometric binaries along the main sequence". In: *aap* 540, A16, A16. DOI: 10.1051/0004-6361/201016384. arXiv: 1111.0552 [astro-ph.SR].

Milone, A. P. et al. (July 2015a). "Multiple stellar populations in Magellanic Cloud clusters - III. The first evidence of an extended main sequence turn-off in a young cluster: NGC 1856". In: *mnras* 450.4, pp. 3750–3764. DOI: 10.1093/mnras/stv829. arXiv: 1504.03252 [astro-ph.SR].

Milone, A. P. et al. (Feb. 2015b). "The Hubble Space Telescope UV Legacy Survey of galactic globular clusters - II. The seven stellar populations of NGC 7089 (M2)*". In: *mnras* 447.1, pp. 927–938. DOI: 10.1093/mnras/stu2446. arXiv: 1411.5043 [astro-ph.SR].

Milone, A. P. et al. (June 2016). "Multiple stellar populations in Magellanic Cloud clusters - IV. The double main sequence of the young cluster NGC 1755". In: *mnras* 458.4, pp. 4368–4382. DOI: 10.1093/mnras/stw608. arXiv: 1603.03493 [astro-ph.SR].

Milone, A. P. et al. (Mar. 2017). "Multiple stellar populations in Magellanic Cloud clusters - V. The split main sequence of the young cluster NGC 1866". In: *mnras* 465.4, pp. 4363–4374. DOI: 10.1093/mnras/stw2965. arXiv: 1611.06725 [astro-ph.SR].

Milone, A. P. et al. (June 2018). "Multiple stellar populations in Magellanic Cloud clusters - VI. A survey of multiple sequences and Be stars in young clusters". In: *mnras* 477.2, pp. 2640–2663. DOI: 10.1093/mnras/sty661. arXiv: 1802.10538 [astro-ph.SR].

Milone, A. P. et al. (Mar. 2020). "The Hubble Space Telescope UV Legacy Survey of Galactic globular clusters - XXI. Binaries among multiple stellar populations". In: *mnras* 492.4, pp. 5457–5469. DOI: 10.1093/mnras/stz3629. arXiv: 2002.06479 [astro-ph.SR].

Mucciarelli, A. et al. (May 2011). "NGC 1866: a milestone for understanding the chemical evolution of stellar populations in the Large Magellanic Cloud". In: *mnras* 413.2, pp. 837–851. DOI: 10.1111/j.1365-2966.2010.18167.x. arXiv: 1012.1476 [astro-ph.SR].

Piotto, G. et al. (Mar. 2015). "The Hubble Space Telescope UV Legacy Survey of Galactic Globular Clusters. I. Overview of the Project and Detection of Multiple Stellar Populations". In: *aj* 149.3, 91, p. 91. DOI: 10.1088/0004-6256/149/3/91. arXiv: 1410.4564 [astro-ph.SR].

Yang, Yujiao et al. (June 2018). "New Insights into the Formation of the Blue Main Sequence in NGC 1850". In: *apj* 859.2, 98, p. 98. DOI: 10.3847/1538-4357/aabe26. arXiv: 1804.03948 [astro-ph.SR].

Zahn, J. -P. (May 1977). "Reprint of 1977A&A....57..383Z. Tidal friction in close binary stars." In: *aap* 500, pp. 121–132.

Zorec, J. et al. (Jan. 2012). "Rotational velocities of A-type stars. IV. Evolution of rotational velocities". In: *aap* 537, A120, A120. DOI: 10.1051/0004-6361/201117691. arXiv: 1201.2052 [astro-ph.SR].